



Geochemistry, Geophysics, Geosystems

RESEARCH ARTICLE

10.1002/2016GC006458

Key Points:

- 3D density distribution in the upper mantle in Asia and surrounding regions
- Joint inversion of different data reveals new features of the lithosphere
- Nature of thermocompositional anomalies in the upper mantle

Supporting Information:

- Supporting Information S1
- Supporting Information S2

Correspondence to:

M. K. Kaban,
kaban@gfz-potsdam.de

Citation:

Kaban, M. K., W. Stolk, M. Tesaro, S. El Khrepy, N. Al-Arifi, F. Beekman, and S. A. P. L. Cloetingh (2016), 3D density model of the upper mantle of Asia based on inversion of gravity and seismic tomography data, *Geochem. Geophys. Geosyst.*, 17, 4457–4477, doi:10.1002/2016GC006458.

Received 26 MAY 2016

Accepted 11 OCT 2016

Accepted article online 17 OCT 2016

Published online 12 NOV 2016

3D density model of the upper mantle of Asia based on inversion of gravity and seismic tomography data

Mikhail K. Kaban^{1,2}, Ward Stolk³, Magdala Tesaro³, Sami El Khrepy^{4,5}, Nassir Al-Arifi⁴, Fred Beekman³, and Sierd A. P. L. Cloetingh^{3,6}

¹German Research Centre for Geosciences (GFZ) Potsdam, Germany, ²Schmidt Institute of Physics of the Earth, Moscow, Russia, ³Utrecht University, Utrecht, The Netherlands, ⁴King Saud University, Riyadh, Saudi Arabia, ⁵National Research Institute of Astronomy and Geophysics, Helwan, Egypt, ⁶Ludwig-Maximilians University of Munich, Germany

Abstract We construct a new-generation 3D density model of the upper mantle of Asia and its surrounding areas based on a joint interpretation of several data sets. A recent model of the crust combining nearly all available seismic data is employed to calculate the impact of the crust on the gravity anomalies and observed topography and to estimate the residual mantle anomalies and residual topography. These fields are jointly inverted to calculate the density variations in the lithosphere and upper mantle down to 325 km. As an initial approximation, we estimate density variations using a seismic tomography model. Seismic velocity variations are converted into temperatures and then to density variations based on mineral physics constraints. In the Occam-type inversion, we fit both the residual mantle gravity anomalies and residual topography by finding deviations to the initial model. The obtained corrections improve the resolution of the initial model and reflect important features of the mantle structure that are not well resolved by the seismic tomography. The most significant negative corrections of the upper mantle density, found in the Siberian and East European cratons, can be associated with depleted mantle material. The most pronounced positive density anomalies are found beneath the Tarim and South Caspian basins, Barents Sea, and Bay of Bengal. We attribute these anomalies to eclogites in the uppermost mantle, which have substantially affected the evolution of the basins. Furthermore, the obtained results provide evidence for the presence of eclogites in the oceanic subducting mantle lithosphere.

1. Introduction

Mass anomalies in the Earth's mantle associated with thermal or compositional heterogeneities produce stresses that initiate mantle convection, plumes, subduction, and deformation of the lithosphere. Therefore, knowledge of the density heterogeneity of the upper mantle is key in understanding its dynamics and role in controlling tectonic processes and surface deformation. This is particularly important in Asia, where nearly all types of tectonic settings are present.

One of the principal issues of upper mantle density modeling is the elimination of the crustal effect from the observed gravity field [e.g., Kaban *et al.*, 2010]. The crust is the most heterogeneous layer in the Earth and its gravitational signal overshadows the signals of other layers, including the upper mantle. On the other hand, the crust has been well studied by various (particularly seismic) methods. Based on these data, it is possible to construct an a priori model of the crust and remove its effect from the observed gravity field. Although attempts were made to calculate mantle gravity anomalies as soon as the first seismic sections were measured, reliable 3D models could not be constructed until sufficient data had been collected on the crustal structure. The first maps of mantle gravity anomalies for a considerable part of North Eurasia were obtained by Artemjev *et al.* [1994]. However, they did not consider the structure of the crystalline crust, which significantly affects the observed gravity field. A next-generation model, based on substantially improved data including the crustal structure, was presented by Kaban [2001]. However, the data used in that study are now largely outdated. Braitenberg *et al.* [2000a,b] inverted gravity data in Qinghai-Tibet to obtain Moho depth variations. Their model implied variations of the lithosphere thickness according to the tomography model of Zhou *et al.* [1991]. However, they did not consider potential changes of the mantle composition. Their study was continued by Shin *et al.* [2007], who used a new gravity field model based on satellite data. Braitenberg *et al.* [2006] also applied gravity inversion to study the structure of the crust and

the elastic thickness of the lithosphere of the South China Sea ridge. In this study, variations of the mantle structure also were not considered. Later, *Bai et al.* [2013] constructed a detailed crustal model based on the gravity data for the Himalayas and Tibet, which again implied a homogeneous upper mantle.

Several studies employed joint inversion of seismic and gravity data to investigate the mantle structure in central Asia [*Maceira and Ammon*, 2009], central Mongolia, and southern Siberia [*Tiberi et al.*, 2008]. These studies attempted to fit both data sets assuming a straightforward relationship between seismic velocity and density. An obvious drawback of this approach is that velocity and density may depend on temperature and composition in different ways. Velocity strongly depends on temperature [e.g., *Goes et al.*, 2000; *Goes and van der Lee*, 2002], whereas density can be equally affected by both factors. A classic example is given by cratonic lithospheric roots, which are characterized by almost no density anomalies because the temperature and compositional effects nearly compensate each other [e.g., *Kaban et al.*, 2003, 2015a] and by very high seismic velocities—owing to low temperatures. Therefore, it is impossible to separate temperature and compositional variations in the upper mantle by using this approach.

Recently, a new high-resolution crustal model was constructed for most of Asia [*Stolk et al.*, 2013]. This model is based on the most complete seismic data set available [*Mooney*, 2010, with updates up to 2015] and uses a revised methodology to interpolate these data. It provides velocity variations and depths of the main crustal boundaries, and it assesses uncertainties in the interpolation. The new crustal model provides, therefore, a basis for more robust gravity models of the upper mantle. Furthermore, new gravity field models have been developed during the last decade that are based on a combination of satellite missions such as GRACE, and Gravity Field and Ocean Circulation Explorer (GOCE) in addition to terrestrial determinations [*Förste et al.*, 2014]. Old gravity models in Asia are often inconsistent and less reliable [*Kaban and Yuanda*, 2014]. Moreover, it is not clear in many cases which corrections have been applied. The new satellite missions provide for the first time homogeneous and high-quality gravity grids for the whole Earth [e.g., *Förste et al.*, 2014]. The difference with older gravity data reaches ± 80 mGal [*Kaban and Yuanda*, 2014], which is far above any acceptable level.

Interpretation methods have also been significantly improved during the last decade. Direct methods for gravity computations include all spherical effects and realistic density distribution. For understanding the structure and dynamics of the lithosphere, it is necessary to first separate the effects of temperature and composition on density variations. In the past, the composition-temperature problem was addressed either by a priori fixing the composition based on xenolith data [e.g., *Goes et al.*, 2000] or by determining the temperature based on surface heat flow [e.g., *Artemieva*, 2009]. In recent years, integral approaches that combine several methods have been attempted [e.g., *Afonso et al.*, 2008]. *Kaban et al.* [2014b] and *Tesauro et al.* [2014a] introduced a new inversion technique that makes it possible to separate upper mantle temperature and compositional anomalies based on joint interpretation of seismic tomography, gravity, and mineral physics data. This technique implies several iterations designed to fit the observed fields by constructing a self-consistent temperature-composition-density model of the upper mantle. As a result, a 3D integrative model of the North American lithosphere has been constructed [*Tesauro et al.*, 2014a, 2015].

The improved technique with new seismic and gravity data sets and seismic tomography data have been recently used for construction of a 3D density model of the lithosphere and upper mantle for the Middle East and surrounding areas [*Kaban et al.*, 2016]. This model gives the possibility of understanding the main factors controlling the density heterogeneity of the upper mantle and, in many cases, clarifying the origin of the ongoing tectonic processes. In the present study, we create a density model of the crust and upper mantle for whole Asia based on improved interpretation methods and updated initial data sets. The integrated 3D model of the lithosphere and upper mantle describes density variations associated with the corresponding temperature and compositional anomalies. In addition, we analyze potential errors of the model related to both uncertainties of the initial data and the technique used. The main improvements compared with previous studies are given in the following points:

1. A new model of the crust [*Stolk et al.*, 2013, with updates up to 2015] is used to estimate the crustal contribution to the observed gravity field and topography.
2. A recent seismic tomography model [*Schaeffer and Lebedev*, 2013, 2014] is inverted for temperature and density to construct an initial density model of the upper mantle.
3. A newly developed inversion technique [*Kaban et al.*, 2014b, 2015a] is employed that utilizes residual gravity anomalies and residual topography to construct a 3D density model of the upper mantle.

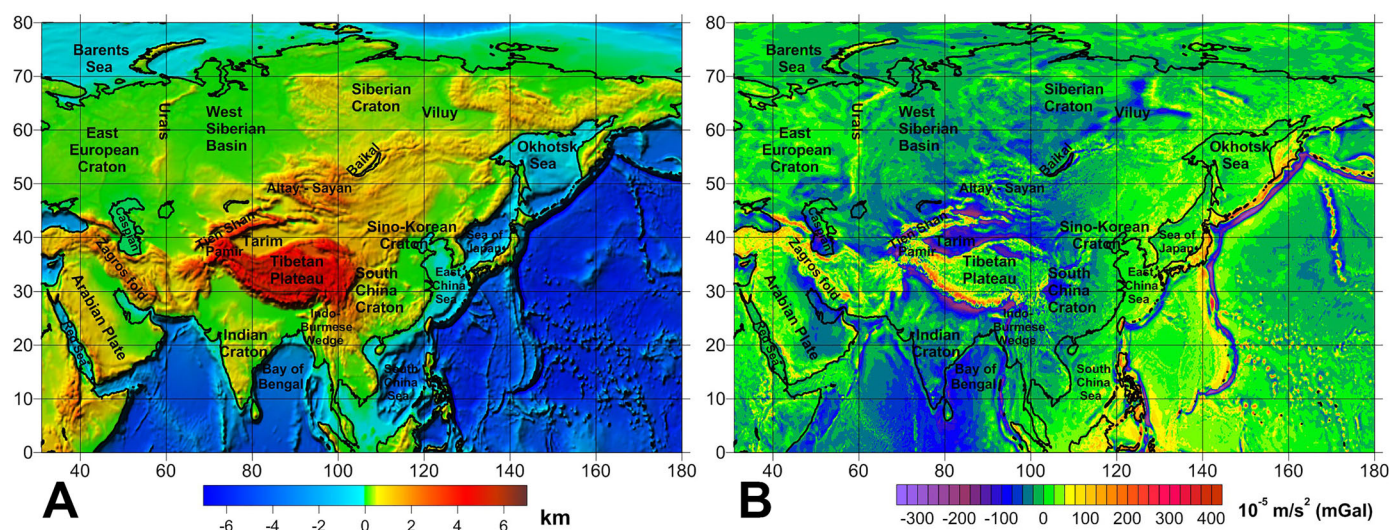


Figure 1. (a) Topography/bathymetry map of the study area with main tectonic units. (b) Free air gravity disturbances determined by model EIGEN-6C4 [Förste *et al.*, 2014].

2. Study Area

The structure of the Asian lithosphere is extremely heterogeneous. To the north, Archean and early Proterozoic crust comprises the Siberian Craton [e.g., Rosen *et al.*, 1994; Griffin *et al.*, 1999] (Figure 1a). Its crystalline basement, made of an association of granites, granulites, gneisses, crystalline schists, and quartzites, with the age ranging from 3.2 to 2.4 Ga, composes the Anabar and Aldan shield, respectively [Nutman *et al.*, 1992; Rundqvist and Mitrofanov, 1993]. During the Devonian a large-scale thermal event occurred in the eastern part of the Siberian Craton, forming (or reactivating) the 600 km long and wide Viluy rift system. The rifting was accompanied by extensive mafic and kimberlite magmatism [e.g., Courtillot *et al.*, 2010]. During the Middle Carboniferous, the Uralian Ocean, which opened in Late Cambrian–Early Ordovician between the Baltica (including the East European Platform) and the Kazakhstanian continent (including the Siberian Craton), closed forming the Uralides [e.g., Puchkov, 2002]. The extension in the Paleozoic initiated subsidence of the West Siberian Basin, one of the largest intracratonic basins of the world, covering an area of 3.5 million km² [e.g., Sengör *et al.*, 1993; Vyssotski *et al.*, 2006], and Barents Sea [Gac *et al.*, 2012] (Figure 1a).

To the south, the assembly of three major Precambrian cratons, the Sino-Korean Craton, South China Craton (composed of the Yangtze Craton and Cathaysia block), and Tarim block form Mainland China [e.g., Zhang *et al.*, 2014]. The Tarim block has a lithospheric structure typical of stable continental platforms [e.g., Maceira and Ammon, 2009] and is separated to the north and south by the Tien Shan and Kunlun Shan mountains respectively, which were accreted from the late Proterozoic to the Cenozoic. The western and eastern parts of the Sino-Korean and South China Craton have experienced very different tectonic histories. The western regions remained stable since the early Proterozoic. Therefore, their lithosphere is largely undeformed and thick (up to >150 km) [e.g., Chen *et al.*, 2009]. In contrast, the eastern parts were significantly affected by the Pacific subduction since the Jurassic. The changes mainly resulted in the craton destruction, which lead to the removal of >100 km of its lowermost lithosphere, widespread volcanism and formation of large-scale sedimentary basins [e.g., Dong *et al.*, 2015]. Furthermore, the subduction of the Pacific and Philippine plates beneath Eurasia lead to the formation of several volcanic arc systems (the Kuril Arc, northeastern and southwestern Japan Arc, Izu-Bonin-Mariana Arc, Ryukyu Arc, and Philippine Arc) and opening of the corresponding back-arc basins (Sea of Okhotsk, Sea of Japan, Philippine Sea, East China Sea, and South China Sea).

The southern part of the Asian continent is dominated by two Cenozoic orogens: the Himalayan-Tibetan orogen in the east, formed by the India-Asia collision, and the Turkish-Iranian-Caucasus orogen in the west, as a result of the Arabia-Asia collision. The evolution of the two orogens was accompanied by shortening in the early stage, followed by strike-slip faulting and extension in the late stage. Farther to the south, the India-Asia collision zone is the most profound ongoing continent-continent collision [e.g., Rowley, 1996]. Beginning at about 50 Ma, the Indian subcontinent collided with Eurasia. India still moves toward Asia at a

relative velocity of 50 mm/yr [White and Lister, 2012]. However, only about 20–25 mm/yr is accommodated by shortening across the Himalayas [e.g., Larson *et al.*, 1999]. The remaining shortening results partly in the southeastward extrusion of crustal material, which was first modeled by Molnar and Tapponnier [1975], and partly in the uplift of the Tibetan Plateau. This convergence caused the formation of the Pamir-Hindukush mountain range to the west and reactivation of older intraplate structures in the Tien Shan and Altay-Sayan mountain regions to the north. These ranges limit to the east the Turan Plate, consisting of an amalgamation of Late Paleozoic to Triassic continental microblocks divided by ocean sutures [Garzanti and Gaetani, 2002] (Figure 1a).

North of the India-Asia collision zone, the Baikal rift began opening on the southeastern border of the Siberian Craton at ~30 Ma [e.g., Petit and Deverchere, 2006; Delvaux *et al.*, 1997]. This feature is about 2500 km long from its southwestern extremity to the northeast and consists of several basins of different ages and geometries [e.g., Logatchev and Florensov, 1978; Petit and Deverchere, 2006]. To the east, the India/Sunda plate's oblique convergence, leading to the subduction of the Bengal crust beneath the Burma sliver plate, resulted in the formation of the Indo-Burmese Wedge [Maurin and Rangin, 2009] (Figure 1a).

In the Turkish-Iranian-Caucasus orogeny zone, the early crustal thickening began around 30–20 Ma. At ~15–5 Ma, it was accompanied by a strike-slip faulting, associated with further northward movement of the Arabian plate, westward extrusion of the Anatolia/Turkey block, and fast extension across the Sea of Crete and Sea of Aegean [Yin, 2010]. The collision between the Arabian plate and Eurasia results in an intracontinental subduction and formation of the Anatolian-Iranian plateau and Zagros Mountains [e.g., Stern and Johnson, 2010]. Further to the north, the collision zone extends to the Caucasus region, including also the Black and Caspian Sea. In contrast, extensional forces, induced by the opening of the northeastern African rifts, associated with the Afar triple junction, the Red sea, and Gulf of Aden, act along the south-southwestern boundary of the Arabian plate. The result of the interaction between the India-Asia and Arabia-Asia collisional processes is a 300–400 km wide and 1500 km long zone of northwest strike-slip faults. This zone extends from the Zagros thrust belt in the southwest to western Mongolia in the northeast and is linked with the active Tien Shan and Altay intracontinental orogens [Yin, 2010] (Figure 1a).

3. Initial Data

3.1. Initial Gravity Field

The gravity field model (EIGEN-6c4) employed in this study is based on a combination of satellite and terrestrial data (Figure 1b) [Förste *et al.*, 2014]. The field is completed up to spherical harmonic degree/order 1949, although this resolution is obtained only in areas with sufficient terrestrial observations that support satellite gravity data. The combination of GRACE and GOCE data allows for the construction of an accurate satellite-only contribution to the final combined model up to degree/order 240 [e.g., Förste *et al.*, 2012, 2014]. This means that the gravity model is independent of the surface data up to a resolution of about 45'. Such resolution is more than that required for this continent-wide study because the maximum resolution of the model is $1^\circ \times 1^\circ$. The initial gravity field is represented by gravity disturbances, which are more appropriate than gravity anomalies for geophysical purposes [Li and Götze, 2001; Hackney and Featherstone, 2003]. Therefore, all derivatives of this field should also be considered as disturbances in a geodetic sense. However, the term "anomalies" is often retained, as is traditionally adopted in geophysical applications.

The Bouguer correction was computed by using the SRTM30_plus model [Becker *et al.*, 2009]. The densities of the topography and sea water were set to 2670 and 1030 kg/m³, respectively.

3.2. Model of the Crust

In this study, a 3D model of the Asian crust was used, as presented in Stolk *et al.* [2013]. The model determines the thicknesses of sediments and three separate layers of the crystalline crust. Each crustal layer is characterized by variations in *P* wave velocity, which are vertically averaged and converted into corresponding density values [Christensen and Mooney, 1995]. All the data are presented on the same $1^\circ \times 1^\circ$ grids related to geographical coordinates.

In the continental area, a sedimentary layer model was compiled mainly from regional maps based on geophysical prospecting studies [Stolk *et al.*, 2013] and supplemented by data from the Exxon Tectonic Map of the World [1985]. Offshore, we employed the detailed model compiled by the National Oceanic and

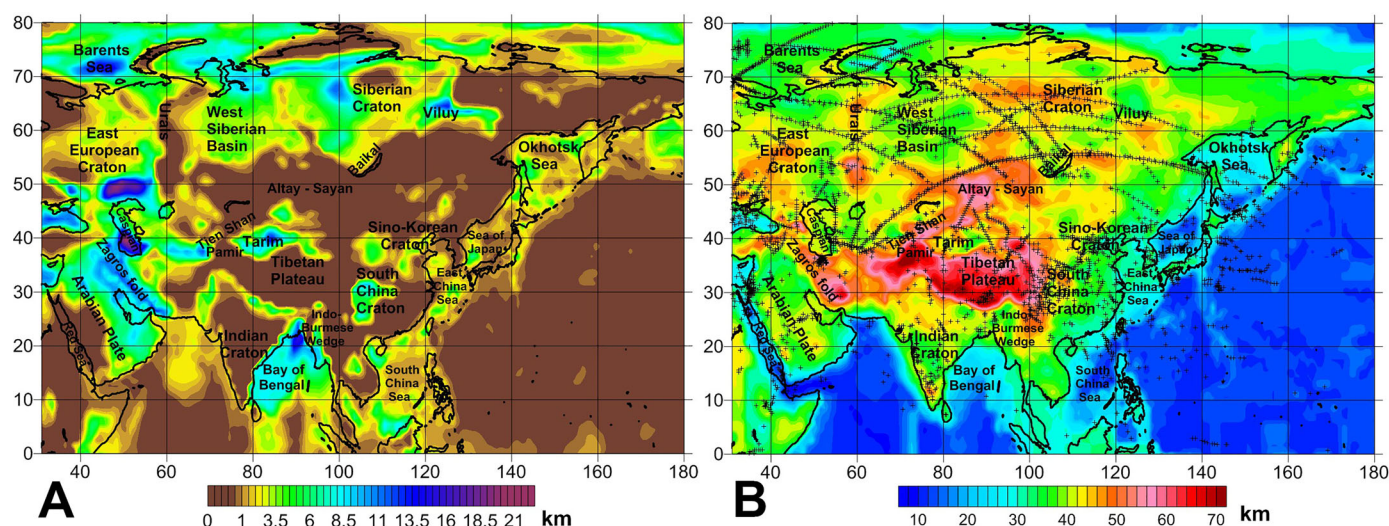


Figure 2. (a) Thickness of sediments in the study region. (b) Depth to the Moho from sea level. Crosses show seismic determinations used for construction of the crustal model.

Atmospheric Administration (NOAA) [Divins, 2003; <http://www.ngdc.noaa.gov/mgg/sedthick/sedthick.html>]. The final model is shown in Figure 2a. Every basin is characterized by specific velocity-depth and density-depth relationships based on available geophysical and geological data [Stolk et al., 2013]. The model was updated for the Middle East region using recent data [Kaban et al., 2015b, 2016].

The crustal model of Asia is based on the most complete data set, which was compiled by the U.S. Geological Survey [Mooney, 2010, with updates up to 2015]. Stolk et al. [2013] proposed a new methodology for determining the depth of the Moho discontinuity in areas with heterogeneous data distribution. The Moho observations were interpolated by using the so-called remove-compute-restore technique, which is also employed in geodesy applications [e.g., Forsberg and Tscherning, 1997]. With this technique, observations are first corrected for Airy-type isostasy. As a result, the residual observations show less variation than the original observations, reducing interpolation uncertainty by 30% or more for many locations [Stolk et al., 2013]. Following the interpolation of residual observations, the isostatic correction that was initially applied is restored to the interpolated depth to the Moho, leading to the final estimate of Moho depth. In this way, it was possible to trace the location of principal features, e.g., mountain ranges, which were sampled by seismic methods just in a few points. It should be noted that this technique helps to interpolate heterogeneous data sets but cannot substitute them. Therefore, for reliability of the results in each specific area we refer to the distribution of the initial data on the crustal structure (Figure 2b). Three relatively large areas, namely the northeastern part of Asia, Indochina and the territories of Afghanistan and Pakistan, are still empty of seismic data; therefore, we do not discuss the results for these areas.

The regional model was embedded in the CRUST1.0 global crustal model [Laske et al., 2013], which was further improved by using detailed compilations of the depth to the Moho and velocities of the crystalline crust in Europe, North America, and Australia [Tesauro et al., 2008; Tesauro et al., 2014b; Collins et al., 2003]. The final Moho model is shown in Figure 2b. The same seismic data were used to determine thickness and velocity/density of the crystalline crust layers including the upper, middle, and lower crusts [Stolk et al., 2013]. The structure of the crystalline crust was estimated by fitting the crustal parameters to the available data at each grid point [Stolk et al., 2013]. The study of Stolk et al. [2013] also determines the interpolation uncertainties for all parameters of the crustal model.

4. Mantle Gravity Anomalies and Residual Topography

The gravity effect of the crust was estimated relative to a laterally homogeneous 1D reference density model consisting of several layers with constant density. Therefore, the crustal correction is equivalent to the Bouguer correction extended from the surface to the Moho [e.g., Mooney and Kaban, 2010]. A different reference model would basically lead to a shift in the average level of the computed gravity anomaly, which is

Table 1. 1D Reference Density Model Used for the Calculation of the Crustal Effect

	Upper Layer	Lower Crustal Layer	Upper Mantle Layer
Depth (km)	0–15	15–40	40–75
Density (kg/m ³)	2700	2940	3357

not considered, but not to the anomalies themselves with respect to that average. The only parameter affecting the results is the reference density of the uppermost mantle. However, this effect is not significant for plausible variations in density [e.g., Mooney and Kaban, 2010]. To enable direct comparison of the results, we used the same reference density employed in global [Kaban *et al.*, 2003] and regional studies [Mooney and Kaban, 2010; Kaban *et al.*, 2014b], as shown in Table 1. Although the reference model is essentially representative of continental areas, it can also be employed in oceanic regions. It is balanced at a depth of 40 km with the old 180 Ma oceanic lithosphere of the cooling plate model [Kaban *et al.*, 1999]. Therefore, although the effects of separate layers can differ, the total gravity effect of the crust is the same.

The gravity anomaly of each layer within the Earth's crust and mantle is calculated by using 3D algorithms for a spherical Earth, considering density changes in the horizontal and vertical directions and the average elevation of each cell. The gravity attraction of each tessieroid elementary volume, limited by the initial horizontal and vertical grid, is computed for all points on the surface. A sum of these vectors gives the vector, which corresponds to the total effect of the crustal layers and ultimately of the entire crust (see for technical details Kaban *et al.* [2015b]). The estimated accuracy of the calculations is within 10^{-5} m/s² (1 mGal), which is significantly less than the effect of the initial data uncertainties.

The gravity effect of distant zones up to the antipodes may be significant [Kaban *et al.*, 2004]. For example, the fundamental differences between the Northern and Southern Hemispheres produce strong trends in all fields. To avoid this problem, the gravity effect of each density boundary or layer, including topography and bathymetry, is calculated for the entire Earth. For these purposes, as was described above, a high-resolution model of the Asian crust was extended for the entire Earth model by using global data sets. The fields created by the sedimentary layer, crystalline crust, and Moho are shown in Figures 3a–3c.

The gravity effect of sediments reaches -110×10^{-5} m/s² (mGal) (Figure 3a). Minimal values are observed in the offshore basins, which are normally filled with young low-density sediments and in the intracontinental basins filled with low-density sediments including extensive salt deposits (e.g., the Pre-Caspian basin). In the continental areas, the effect depends not only on thickness but also on the type of sediment, which is characterized by specific density-depth relationships [Stolk *et al.*, 2013]. For example, “hard” basins within the Siberian Craton, which contain large trap sequences, with high velocity/density material up to 6–8 km thick produce only insignificant gravity signals up to -30×10^{-5} m/s². In contrast, the effect of soft basins is significant and may exceed -100×10^{-5} m/s² (Figure 3a). These basins are characterized by similar or larger thicknesses of sediments with low velocity/density values such as the West Siberian basin and basins associated with the Caspian Sea.

The gravity field produced by the crystalline crust is even more significant, in the range of about -160 to 350×10^{-5} m/s² (mGal; Figure 3b). It depends not only on an average density of the crust but also the depth to the basement and the Moho. In the case of thick sediments, the average reference density of the crust is increased, up to 2940 kg/m³ (Table 1); thus, the effect of the crystalline crust is decreased (e.g., South Caspian, Barents, and Okhotsk Seas, Figure 3b). The same occurs in the case of deep Moho depth (e.g., Tibet). The Moho depth variations produce the largest effect on the gravity field (Figure 3c), which ranges from about -260 to more than 800×10^{-5} m/s² (mGal) and clearly correlates with the Moho variations (Figure 2b).

In addition to the residual mantle anomalies, we estimated the residual topography (t_{res}), which is part of topography that is not balanced by the crust in an isostatic sense, according to the crustal density model [e.g., Kaban *et al.*, 2004]:

$$t_{res} = \frac{1}{\bar{\rho}} (\rho_{top}) t_{obs} + \frac{1}{\bar{\rho}} \int_0^M \Delta\rho(h) \left(\frac{R-h}{R} \right)^2 dh, \quad (1)$$

where ρ_{top} is the average block density of topography including the effects of ice and sediments (t_{obs}); $\bar{\rho} = 2670$ kg/m³ is the average density of t_{res} ; $\Delta\rho(h)$ is the density anomaly including water, relative to the horizontally homogeneous reference model; t is the topography height, which is zero for sea areas; h is the

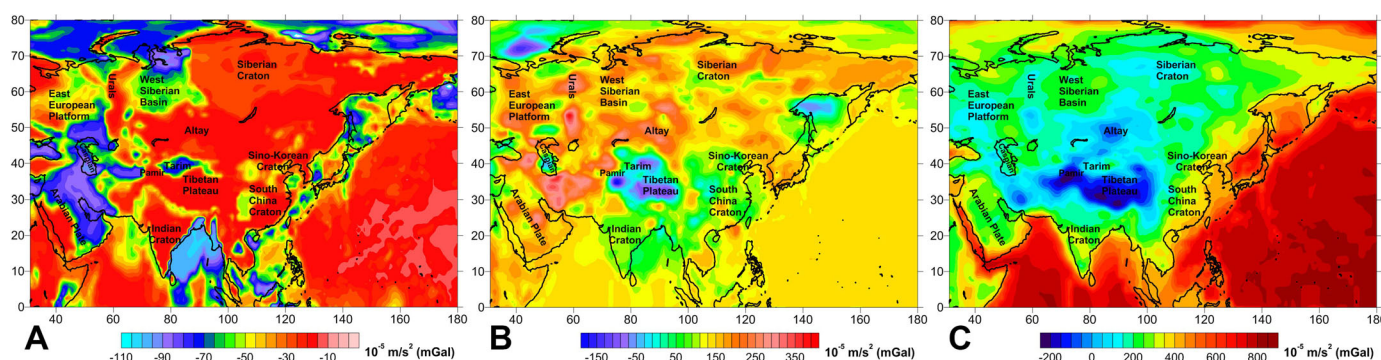


Figure 3. Gravity effect of the crustal layers relative to the reference density model: (a) sediments, (b) crystalline crust, and (c) Moho.

depth below the geoid; and R is the radius of the Earth. The integration is limited to the Moho because below this boundary, $\Delta\rho(h)$ is assumed to be zero at this stage.

The residual topography is an important parameter often used in geophysical studies, particularly in dynamic modeling [Boschi *et al.*, 2010; Faccenna and Becker, 2010; Ghosh *et al.*, 2013]. Three main factors responsible for the residual topography should be considered [Kaban *et al.*, 2004]. The first is the effect of isostatic disturbances, including deflections from the local isostatic model, and the corresponding stress field in the lithosphere, which are dominant at relatively short wavelengths compared with those in the continent-wide study. The long-wavelength anomalies associated with retained postglacial deformation have relatively low amplitudes of several tens of meters. The second factor relates to the lithosphere density heterogeneity below the Moho, which is not considered at this stage. In this way, high-density lithospheric keels of the old continental lithosphere control near-zero topography, whereas the low-density lithosphere pushes up the topography. The third component of the residual topography is the normal stresses acting at the base of the lithosphere and induced by mantle flow (dynamic topography).

The main aim of this study is to identify the anomalous density distribution in the upper mantle. Therefore, it is necessary to eliminate the impacts of other factors. Local isostatic disturbances can be filtered out to some extent by considering only midscale or large-scale anomalies. The effect of the deep mantle on t_{res} can be calculated by using global convection models. In this study, we employed the same global dynamic model used by Kaban *et al.* [2015a, 2016], which provides the effects of deep density anomalies below 325 km (bottom of the upper mantle model in this study). This model includes the effect of lateral variations of viscosity, weak plate boundaries, and the density variation related to the phase transition boundaries [Kaban and Trubitsyn, 2012; Petrunin *et al.*, 2013; Kaban *et al.*, 2014a]. More details on these calculations and maps of the gravity field and dynamic topography, induced by the density heterogeneity below 325 km, are provided in the supporting information [Gu *et al.*, 2003; Kaban *et al.*, 2014a; Flament *et al.*, 2013]. Before the inversion, the impact of deep layers was also removed from the residual mantle anomalies. Therefore, the remaining fields reflect the effect of the heterogeneity of the lithospheric and sublithospheric mantle up to a depth of 325 km.

The residual mantle gravity anomalies and residual topography calculated by removing the effects of the crust from the observed fields are shown in Figures 4a and 4b. The mean value of the gravity anomalies is not interpretable and was set to zero for the study area because it depends on the choice of reference model and distribution of anomalous masses over the entire Earth. In contrast, the absolute values of the residual topography were retained, which are directly related to the balance of the reference crust-mantle column.

Mooney and Kaban [2010] reviewed the potential errors of the residual gravity anomalies and residual topography. At the present-day, the gravity field model is sufficiently robust [Förste *et al.*, 2014]; and the main uncertainty is related to the uncertainties of the crustal model. Considering only large-scale anomalies of at least several hundreds of kilometers, Mooney and Kaban [2010] concluded that the uncertainty related to the gravity effect of sediments may reach $\sim 15\%$, which corresponds to about $15 \times 10^{-5} \text{ m/s}^2$ (mGal) for thick and low-dense basins. Small-scale deviations (e.g., salt domes or basaltic intrusions) might produce more significant effect, but we leave them for regional and local studies. The error due to the uncertainty in

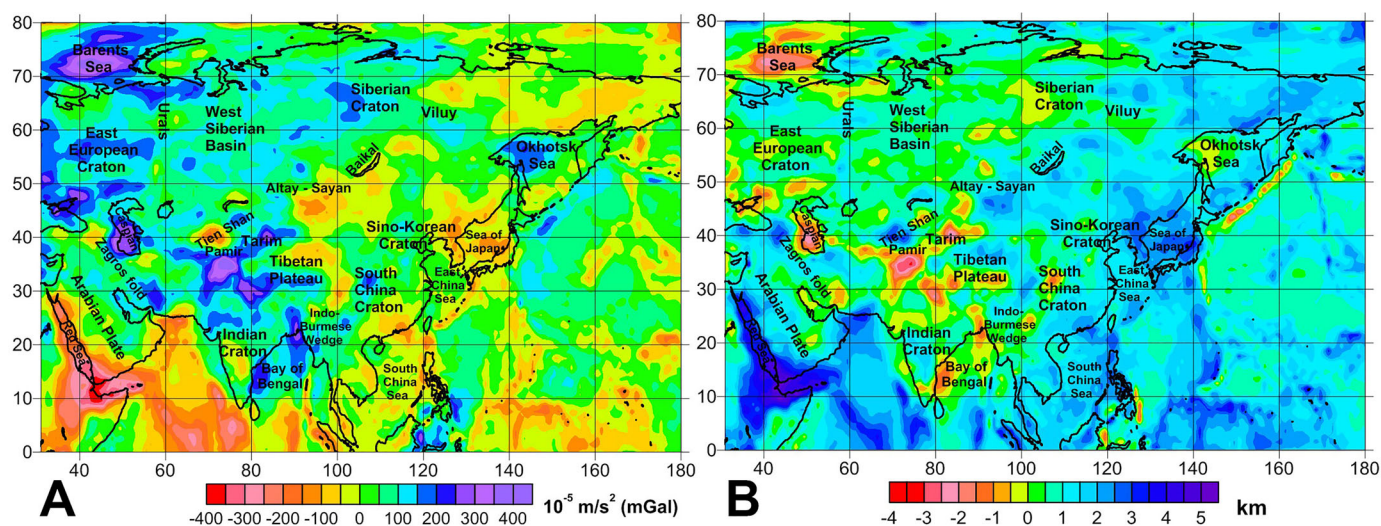


Figure 4. (a) Mantle gravity anomalies and (b) residual topography obtained by removing the crustal effects from the observed fields. The density of the residual topography is 2670 kg/m^3 .

the Moho depth may vary from about $30 \times 10^{-5} \text{ m/s}^2$ for the areas well covered by seismic determinations (ca. >10 points) to approximately $60 \times 10^{-5} \text{ m/s}^2$ in active tectonic regions and not well-studied areas. For the effect of the crystalline crust, we consider uncertainties provided by *Christensen and Mooney* [1995] for the velocity to density conversion. This effect may reach $25\text{--}50 \times 10^{-5} \text{ m/s}^2$; the minimum value corresponds to the thin crust ($\sim 20 \text{ km}$) and maximum—for the thick one ($40\text{--}50 \text{ km}$).

Considering possible combinations of all sources, the total uncertainty, or standard deviation, of the residual crust-free gravity ranges from about $40 \times 10^{-5} \text{ m/s}^2$ (mGal) in the areas well-covered by high-quality seismic data of crustal structure, to about $75\text{--}100 \times 10^{-5} \text{ m/s}^2$ for areas with thick crust and sparse seismic data [Mooney and Kaban, 2010]. The corresponding uncertainty of the residual topography varies from ~ 0.35 to $\sim 0.65\text{--}0.85 \text{ km}$, respectively. Assuming that typical anomalies in the upper mantle extend for about 100 km (see the results below), the corresponding uncertainties of the computed density variations could span from 10 to $20\text{--}24 \text{ kg/m}^3$ at most respectively. As mentioned before, some parts of Asia such as Afghanistan, Pakistan, and the northeastern region adjacent to the Siberian Craton are almost uncovered by seismic data (Figure 2b). For this reason, the results obtained in these areas are not discussed in this study.

The maximum amplitude of the residual gravity anomalies is about $\pm 400 \times 10^{-5} \text{ m/s}^2$, and the residual topography spans from about -4 km to more than 5 km . Therefore, the largest anomalies well exceed the uncertainties. Obviously, these two fields are mirrored (Figures 4a and 4b), which is logical because the low-density lithosphere supports elevated topography and vice versa. Thus, for description of the main anomalies, we consider the gravity field only. However, the differences between these parameters are important, as it will be demonstrated in the following stage, when we construct a 3D density model of the upper mantle.

The most significant negative mantle gravity anomalies (and maxima of the residual topography) are associated with areas characterized by intensive mantle upwelling at a minimum of $-480 \times 10^{-5} \text{ m/s}^2$ over the Afar triple junction (Figure 4). The Afar anomaly further extends to the Red Sea and the Gulf of Aden and continues toward the Carlsberg Ridge. In eastern and southeastern Asia, pronounced minima correspond to back-arc basins, such as to the Sea of Japan and the South China Sea. The Sea of Okhotsk in the north is clearly characterized by a dipole-type structure. A gravity minimum occurs in the southeastern part adjoining the Kurile arc, whereas a strong maximum is present in the northwestern part (Figure 4a). Because the crustal structure in the Sea of Okhotsk is well constrained by seismic data (Figure 2b), these anomalies are robust. Another strong maximum, exceeding $400 \times 10^{-5} \text{ m/s}^2$, occurs in the Barents Sea near the northwestern corner of Asia. Although the mantle anomalies in Asia show complicated patterns, some general tendencies are observed. Negative gravity anomalies dominate in Southeast Asia east of Tibet and the

Tarim basin (Figure 4a). In the northwest, the boundary between predominantly positive and negative anomalies extends from Altay along the northwestern boundary of the Sayan Mountains toward the Baikal rift zone and further to the north boundary of the continent east of the Siberian Craton. We will discuss these fundamental differences after the construction of a 3D density model of the mantle. In agreement with previous studies [Kaban *et al.*, 2016], we detected a very strong positive anomaly over the South Caspian basin. Different anomalies characterize intracontinental plate boundaries. Some, such as the boundary of the Himalayas with the Northern Tibetan plateau and the southern Pamir Mountains, are associated with strong positive anomalies. Others, such as the Zagros fold belt are not observed in the residual gravity and topography field (Figure 4a). Differences are also present between the cratons. The Siberian and East European cratons are characterized by strong positive mantle gravity anomalies, whereas near-zero or negative values prevail in the Indian, South China, and Sino-Korean cratons.

The strong variations in mantle gravity anomalies and residual topography provide evidence for the strong density heterogeneity of the upper mantle in Asia and its surrounding areas. In the following section, we analyze these fields together with other data (mainly seismic tomography) and create a 3D density model of the upper mantle. In particular, this model should indicate which factors are responsible for the density variations.

5. Initial Thermal and Density Model of the Uppermost Mantle

The initial temperature-density model of the upper mantle is based on the SL2013sv global tomography model [Schaeffer and Lebedev, 2013, 2014]. SL2013sv provides variations of vertically polarized shear-wave velocities (V_s) for the upper mantle and transition zone. For conversion of seismic velocity into density, we used the same method as that previously employed for North America [Kaban *et al.*, 2014b; Tesaura *et al.*, 2014a] and the Middle East [Kaban *et al.*, 2016]. The initial temperatures and densities were computed globally in the uppermost mantle up to a depth of 325 km by using the approach of Stixrude and Lithgow-Bertelloni [2005]. In the initial model, the composition is the same throughout the entire uppermost mantle, specifically the Primitive Mantle, which consists of 58.5% olivine, 11.5% clinopyroxene (CPX), 15.0% orthopyroxene (OPX), and 15.0% garnet [McDonough and Sun, 1995]. The attenuation model Q4 of Cammarano *et al.* [2003] was applied for the anelastic correction. The temperature variations at depths of 100, 150, and 200 km in the study area are shown in Figure 5.

The initial thermal model (Figures 5a–5c) may contain significant inaccuracies related to uncertainties of the tomography model and limitations of the velocity-to-temperature conversion. Tomography models do not usually provide direct estimations of velocity uncertainties, which depend on numerous factors including the crustal correction applied, the reference seismic model used, and inhomogeneous ray coverage [e.g., Foulger *et al.*, 2013]. Therefore, it is difficult to estimate these uncertainties and thus assess the reliability of the seismic tomography model. According to Schaeffer and Lebedev [2013], SL2013sv can be used to identify features less than 6 arc degrees globally and significantly smaller in well-sampled continental regions. Therefore, at this stage, we limited our analysis to anomalies larger than several hundreds of kilometers. In the following joint

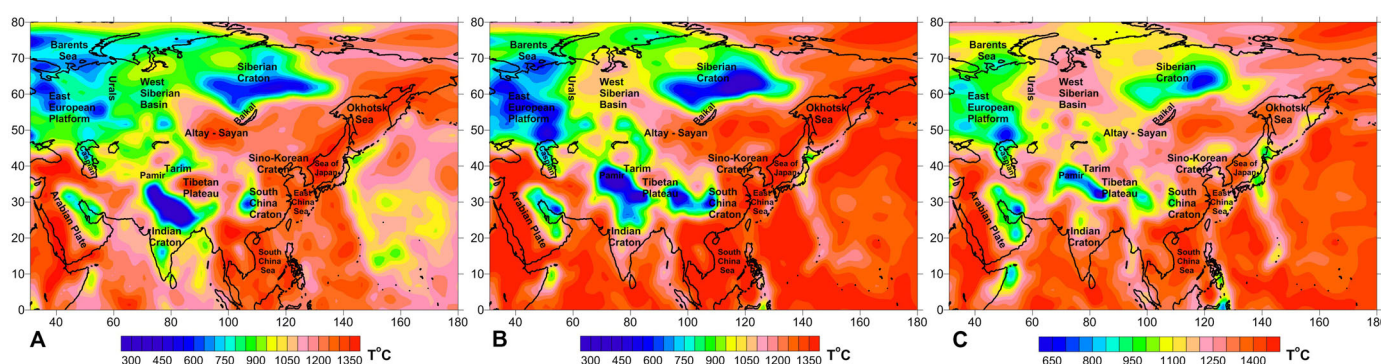


Figure 5. Initial thermal model of the uppermost mantle. Temperatures variations are shown at depths of (a) 100 km, (b) 150 km, and (c) 200 km.

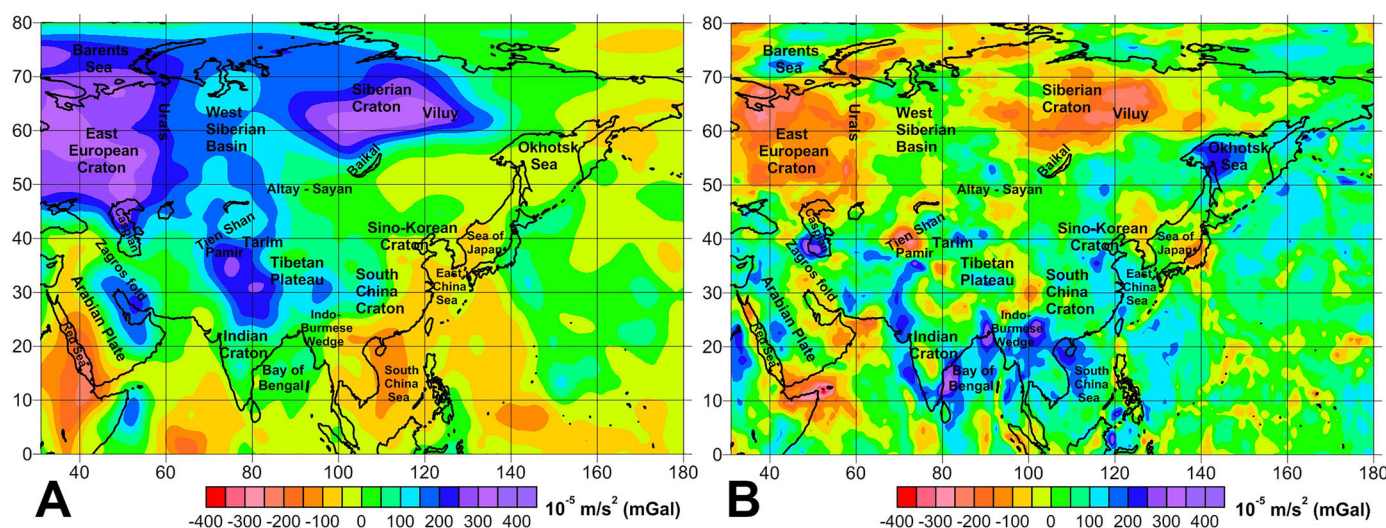


Figure 6. (a) Gravity effect of the initial thermal model of the mantle and (b) residual gravity anomalies obtained by removing this effect from the total mantle gravity field shown in Figure 4a.

inversion with the residual gravity field and residual topography we aim to improve the resolution of the initial model and correct possible uncertainties. The effect of composition is also discussed below.

The initial temperature model shows a clear distinction of the cold lithosphere at 100 km in depth under the East European and Siberian cratons and the Himalayan convergence zone, as opposed to the warmer lithosphere to the south and east of the Tien Shan and Altay Mountain ranges (Figure 5a). At a depth of 150 km, the shape of the cold blocks remained similar, although the Himalayan block shifted to the north, reflecting the location of the subducting lithosphere (Figure 5b). This positive anomaly further extends to the Pamir Mountains to the west and to the North China Craton to the east. The West Siberian Basin becomes remarkably warmer at this depth. At larger depth of 200 km (Figure 5c), the relatively cold lithosphere still underlies the Siberian Craton and East European Platform. A remarkable feature is the warm mantle beneath the Sino-Korean Craton, which reflects the lack of a lithospheric root [e.g., *Griffin et al.*, 1998; *Zheng et al.*, 1998]. The cold mantle to the east of Japan is related to the subducting Pacific plate. The subsequent inversion with the residual gravity and topography should reveal zones in the mantle, in which the initial assumptions on the composition of the upper mantle are not correct.

The initial density model mirrors the temperature field; therefore, it is not displayed here. The gravity effect of the thermal model is shown in Figure 6a. The reference density values employed in the calculations are listed in Table 2. They represent the global averages based on the temperatures estimated by conversion of seismic velocities (Figures 5a–5c), assuming the “fertile” composition of the upper mantle [*Tesaro et al.*, 2014a]. The gravity effect of the temperature variations was estimated in the same way as for the crustal layers taking into account all spherical effects. Compared with the temperature maps shown in Figures 5a–5c, the gravity thermal anomalies mainly reflect the fundamental differences between the cold lithosphere of the northern cratons and the hot upper mantle beneath the western and southern parts of the continent. Intracontinental plate collision zones such as the Zagros and Himalayan fold belts also produce strong gravity effects. Small-scale details are somewhat reduced owing to their deep location. After removing the gravity effect of the thermal anomalies from the residual mantle anomalies, we obtained the field shown in Figure 6b. Although the thermal model represents only a first iteration, we refer to this field as temperature corrected (TC) mantle gravity anomalies and residual topography. The following factors should be considered when interpreting the TC mantle gravity anomalies [*Kaban et al.*, 2015a, 2015b, 2016]:

Table 2. 1D Reference Density Model of the Upper Mantle Below 75 km

Depth (km)	100	150	200	250	300
Density (kg/m ³)	3384	3419	3457	3510	3560

1. Compositional variation in the upper mantle rocks is likely the most important factor. Seismic velocities and density depend on temperature and composition in different ways. Thus, density anomalies do not necessarily correlate with velocity variations [e.g., *Anderson and Bass*, 1984]. A clear example is given by eclogites, which have nearly the same seismic velocities, but significantly higher densities as those of the upper mantle peridotites.
2. The velocity-temperature conversion may be biased by several factors that are not considered, such as composition and volatiles, and also by uncertainties of the model parameters (e.g., the anelastic model).
3. Uncertainties of the seismic tomography model, including insufficient resolution and damping, lead to smearing of anomalies and decreases in their amplitude.
4. Uncertainty in the crustal model used for gravity and topography corrections.

In this study, we cannot completely differentiate these effects. Therefore, we should consider all of them while interpreting the residual anomalies and the density model, which is based on the inversion of all fields. Some preliminary conclusions can be made based on several reasons. First, the wide anomalies in the stable and cold continental interiors cannot be attributed to the uncertainties of the tomography model or to the effect of volatiles. Second, the crustal model is also based on many robust seismic determinations in most of these areas. Therefore, the strong negative anomalies of less than $-200 \times 10^{-5} \text{ m/s}^2$ over the East European and Siberian cratons indicate depleted mantle, which is in agreement with previous studies [e.g., *Griffin et al.*, 1999; *Kaban et al.*, 2003; *Artemieva et al.*, 2006]. Several sedimentary basins, particularly the South Caspian basin, Bay of Bengal, western part of the Okhotsk Sea, and Barents Sea, are characterized by strong positive anomalies of greater than $200 \times 10^{-5} \text{ m/s}^2$, which are likely associated with eclogite bodies, as previously suggested by *Ebbing et al.* [2007], *Braitenberg and Ebbing* [2009], and *Gac et al.* [2012]. On the contrary, the unexpected presence of positive anomalies in the southwestern Pacific Ocean can be likely attributed to volatiles in the upper mantle, because their effect has not been considered when we performed the velocity-temperature conversion. Uncertainties in the initial tomography and crustal models could also be responsible for many local anomalies in the TC mantle gravity field (Figure 6b). In the following section, we develop a 3D density model of the mantle that fits these anomalies, and we discuss a possible origin of the revealed density variations.

6. 3D Density Model of the Upper Mantle

The residual mantle gravity anomalies reflect the effects of density variations in the upper mantle induced by both thermal and compositional changes. However, construction of a reliable 3D model based only on these anomalies is impossible because the inverse gravity problem is essentially ill-posed. The problem of determination of the density distribution ρ may be formulated as shown in *Kaban et al.* [2015a]:

$$\min \{ \|A\rho - g_{\text{res}}\|^2 + \alpha\Omega(\rho) \}, \quad (2)$$

where \mathbf{A} is the integral operator converting density into the gravity field. The operator \mathbf{A} has no continuous inverse \mathbf{A}^{-1} ; thus, a direct solution is neither unique nor stable. To overcome this principal weakness, a so-called regularization term Ω is added [Tikhonov and Arsenin, 1977], where α defines the strength of regularization. The regularization may imply a reference density model based on a priori information such as seismic tomography data [e.g., *Basuyau et al.*, 2013].

The computed residual topography opens additional possibilities for constraining a 3D density structure of the upper mantle. Both residual gravity and residual topography depend on the same factors but essentially in different ways depending on the size and depth of their anomalies [Kaban et al., 2015a]. Therefore, using both parameters provides a possibility for resolving the vertical stratification of the density anomalies. The inverse problem is then reformulated as:

$$\min \{ \|A\rho - g_{\text{res}}\|^2 + k\|B\rho - t_{\text{res}}\|^2 + \alpha\|\rho - \rho_{\text{ini}}\|^2 \}, \quad (3)$$

where \mathbf{B} is the integral operator converting density in topography perturbations and $\mathbf{k} = 2\pi\mathbf{G}\rho_t$ is the scaling coefficient normalizing topography and gravity. The regularization condition implies that the obtained density structure should be close to a predefined model. If such a model is not available ($\rho_{\text{ini}} = 0$), the obtained density perturbations should be minimal, implying Occam-type inversion. The inversion is performed in a spherical harmonic domain, where the solution can be found separately for each spherical

coefficient [e.g., *Forte and Peltier*, 1991]. The integral operator **B** converting density variations in the upper mantle into topography perturbations is computed by using a predefined viscosity model of the mantle. Although, this parameter is quite uncertain, it has been demonstrated by *Kaban et al.* [2015a] that plausible variations of the viscosity profile do not affect remarkably the obtained result, because the topography kernels (operator **B**) are less sensitive to viscosity for the uppermost mantle density variations than for the deep mantle.

This inversion technique has been extensively tested [*Kaban et al.*, 2015a supplementary]. It has been demonstrated that this technique can be used to reconstruct initial density patterns including various combinations of positive and negative anomalies, which reproduce the density distribution in typical tectonic settings. However, the amplitude could be reduced by damping, which leads to some smearing of the computed density anomalies. Therefore, it is important to have a realistic initial model that provides additional constraints. In this study, we employed the initial density distribution, which is based on the tomography model of *Schaeffer and Lebedev* [2013].

We used the same model setup that has been previously employed for the study of the North American lithosphere and upper mantle [*Kaban et al.*, 2015a]. Solutions were found for seven layers with boundaries at depths of 0, 25, 75, 125, 175, 225, 275, and 325 km. The uppermost layer and part of the second layer were used for correction of the crustal model. Therefore, the effect of possible uncertainties in the initial crustal model is partially eliminated by determining additional perturbations to the average density of the crust. Layers 2–7 provide corrections for the initial density model of the mantle based on seismic tomography. Equation (3) was solved in a spherical harmonic domain, which significantly simplified the calculations [*Kaban et al.*, 2015a, 2016]. The model for Asia was embedded in the global model as described above. Although the data outside the study area are less reliable, they are sufficient to describe long distant effects, e.g., related to the fundamental difference between the southern and northern hemisphere or to the effects of the continents and oceans. A solution was found up to the 180th spherical harmonic degree/order. The mantle viscosity profile of *Steinberger and Calderwood* [2006] was used to compute the topography undulations. For additional details and numerical tests proving the stability of the solution for possible variations of the model parameters, we refer to *Kaban et al.* [2015a, supplementary materials]. It should be noted that the zero term may not be determined in this procedure. Therefore, we discuss only the variations of the calculated densities, not their absolute values.

The calculated density variations are shown in Figures 7 and 8. The obtained model perfectly fits both fields of the mantle gravity anomalies and residual topography. The misfit of the gravity field ranged from -19 to $14 \times 10^{-5} \text{ m/s}^2$ (mGal) with a root-mean-square (rms) error of $2.4 \times 10^{-5} \text{ m/s}^2$, which is more than one order less than the initial amplitude (Figure 5b). Deviations of the computed topography ranged from -0.09 to 0.07 km with an rms of 0.014 km, which represents the same proportion to the initial field as that of the gravity deviations because both parameters were properly scaled in the inversion in equation (3). The corrections to the initial model are significant and reached about $\pm 50 \text{ kg/m}^3$ (Figures 7 and 8). However, due to the damping, the computed anomaly might be underestimated by about 30% [*Kaban et al.*, 2015a]. Therefore, these results should be considered as a lower limit, while actual density variations may reach $\sim 65 \text{ kg/m}^3$. The horizontal resolution of the final density model is remarkably improved compared to the initial model based on the seismic tomography. However, some small-scale density fluctuations in the uppermost mantle layer could be a result of a “smearing” of the errors associated with the crustal correction. Due to the damping, these anomalies might extend in the upper mantle, as likely in the case of the Siberian and European cratons (Figures 7b and 7c, depth 100 km).

The most extended negative corrections are related to the East European Platform and the Siberian Craton (Figure 7b). They are significant at all depths down to 250 km and reflect the effects of the mantle depleted in heavy constituents (e.g., garnet), which is thus less dense than a fertile mantle under the same pressure and temperature (P-T) conditions [*Jordan*, 1978, 1988]. The temperature in these cratons could have been underestimated owing to differences in composition [*Tesauro et al.*, 2014a]. However, a temperature increase of about 100°C would raise the density correction up to about 10 kg/m^3 , which is significantly lower than the computed anomalies (Figure 7b). Both the East European and Siberian cratons are well constrained by the initial data. Therefore, the calculated negative anomalies (corrections) are related to the compositional changes in the upper mantle owing to depletion. Their amplitude reaches $\sim 45 \text{ kg/m}^3$, which is less than the value previously predicted in a global study based on only the gravity field (60 kg/m^3)

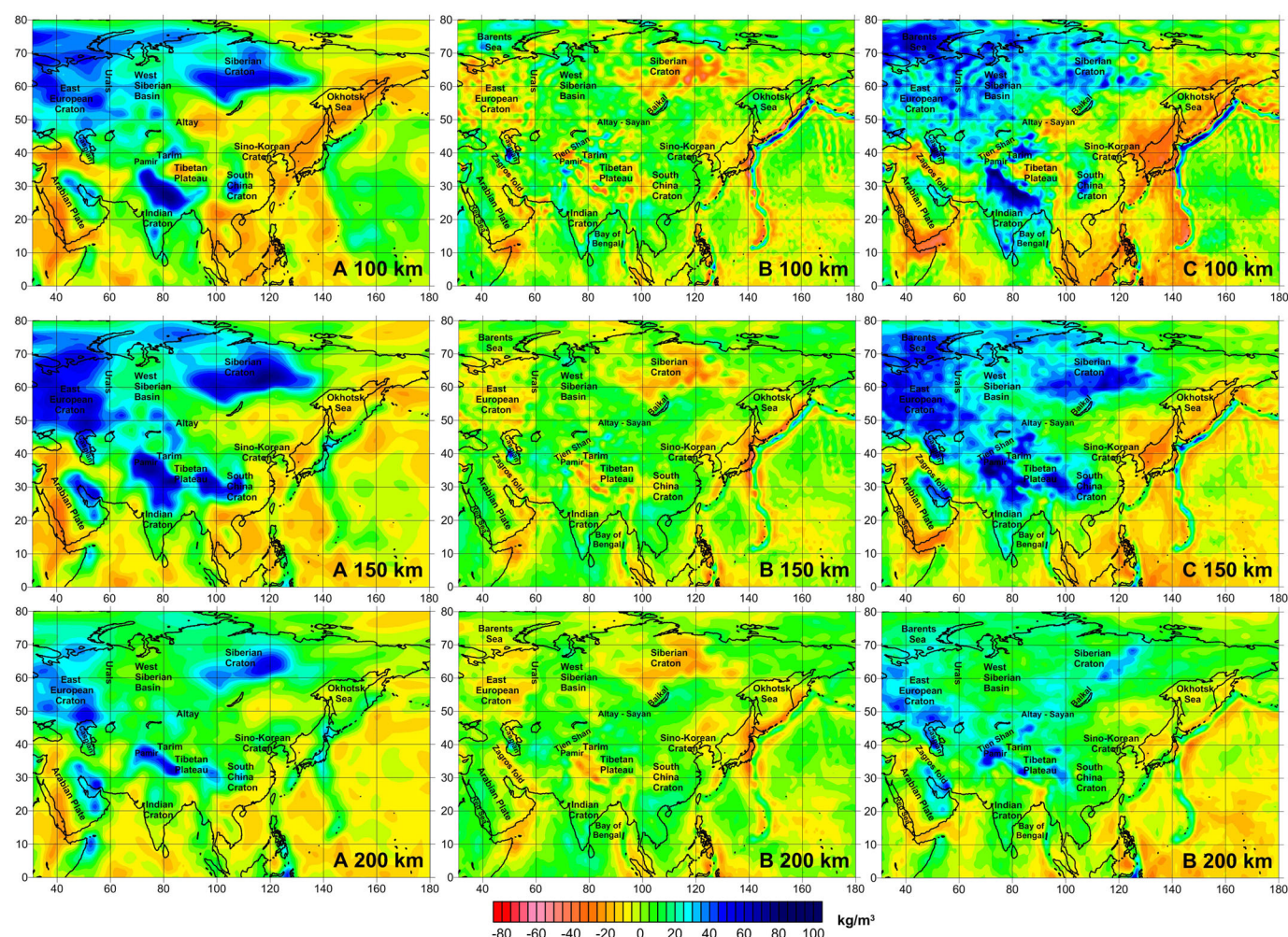


Figure 7. Density variations in the upper mantle at depths of 100, 150, and 200 km according to the constructed 3D density model. (a) Initial density variations obtained from the temperature variations shown in Figure 7. (b) Corrections to the initial model obtained by joint inversion of the residual thermally corrected mantle gravity field and residual topography. (c) Adjusted density variations that fit both the residual gravity field and topography and have minimal deviations from the initial model.

[Kaban *et al.*, 2003]. This difference could be a result of the damping in the inversion. The maximum correction, up to about -50 kg/m^3 , was obtained at a depth of 100 km within the Siberian Craton and corresponds to the western part of the Viluy basin, Lower Lena basin, and Anabar Shield (Figure 7b). The correction was insignificant for the Tunguska basin and Putorana Plateau, located in the western part of the Siberian Craton, which are characterized by extensive trap magmatism [Griffin *et al.*, 1999, 2005]. To discuss in details the final density distribution for major tectonic structures, we display several cross sections showing the initial density variations, corrections, and the final density model (Figure 8). One of the principal features of the model is that the lithosphere-asthenosphere boundary (LAB) is not presented everywhere as a pronounced density contrast. It often represents an extended gradient zone, which, therefore, is not well resolved by seismic tomography and also not in the density structure after the inversion. It is visible only in the areas characterized by a strong temperature contrast, e.g., under some cratons and in plate convergence zones.

The Siberian Craton is characterized by a very strong initial density anomaly that corresponds to the largest S-wave velocity values (Figure 8, cross-sections 1 and 2). However, after the inversion of the residual gravity and residual topography, this positive anomaly was compensated to a large extent by the density decrease, which is likely related to depletion. The compensation was not uniform. In the central part of the craton, it extends to a depth of about 250 km, whereas it is limited to the uppermost mantle in the southeastern region including the Aldan Shield. The density decrease reached a maximum of about 45 kg/m^3 (1.35%) in

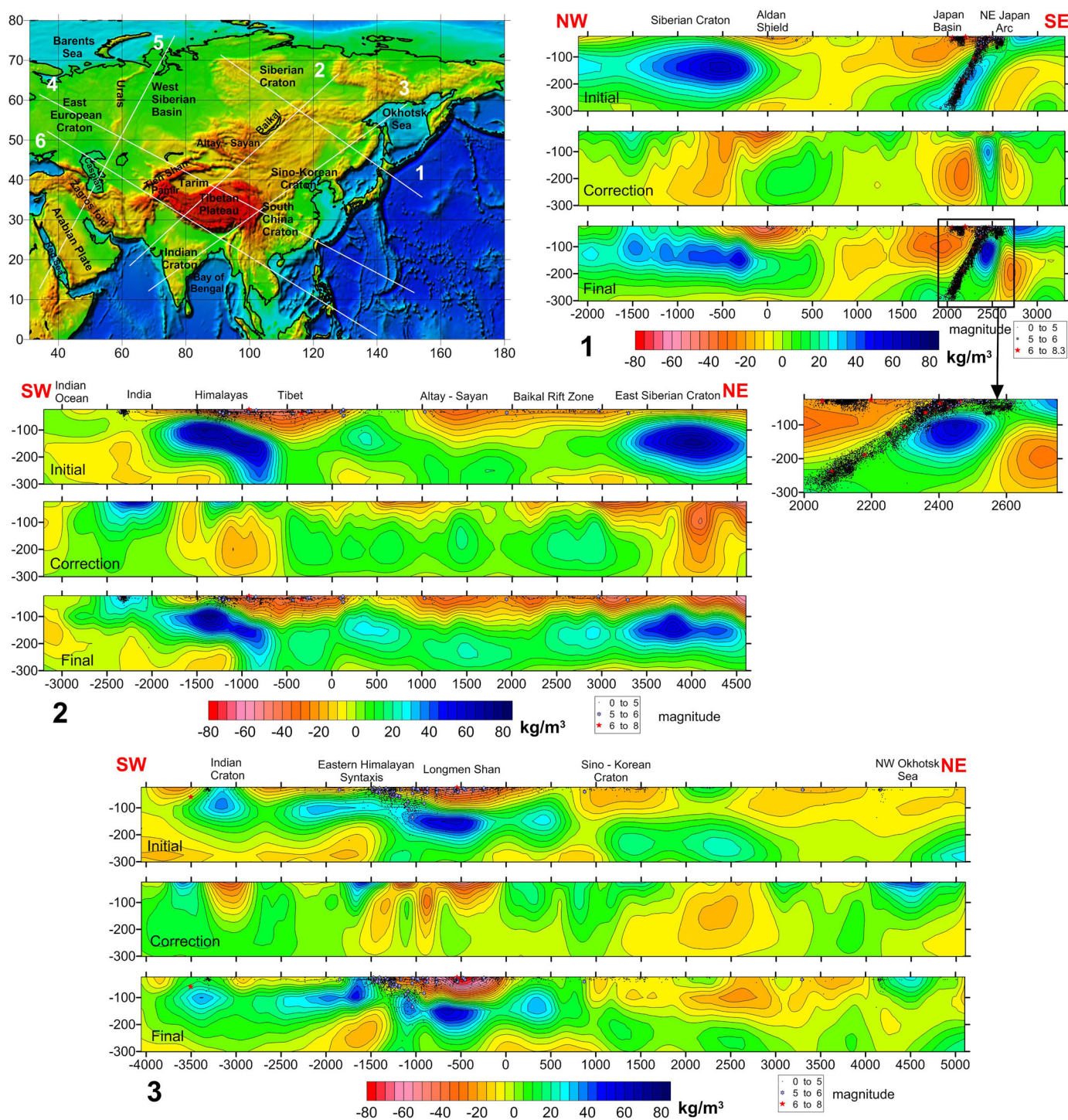
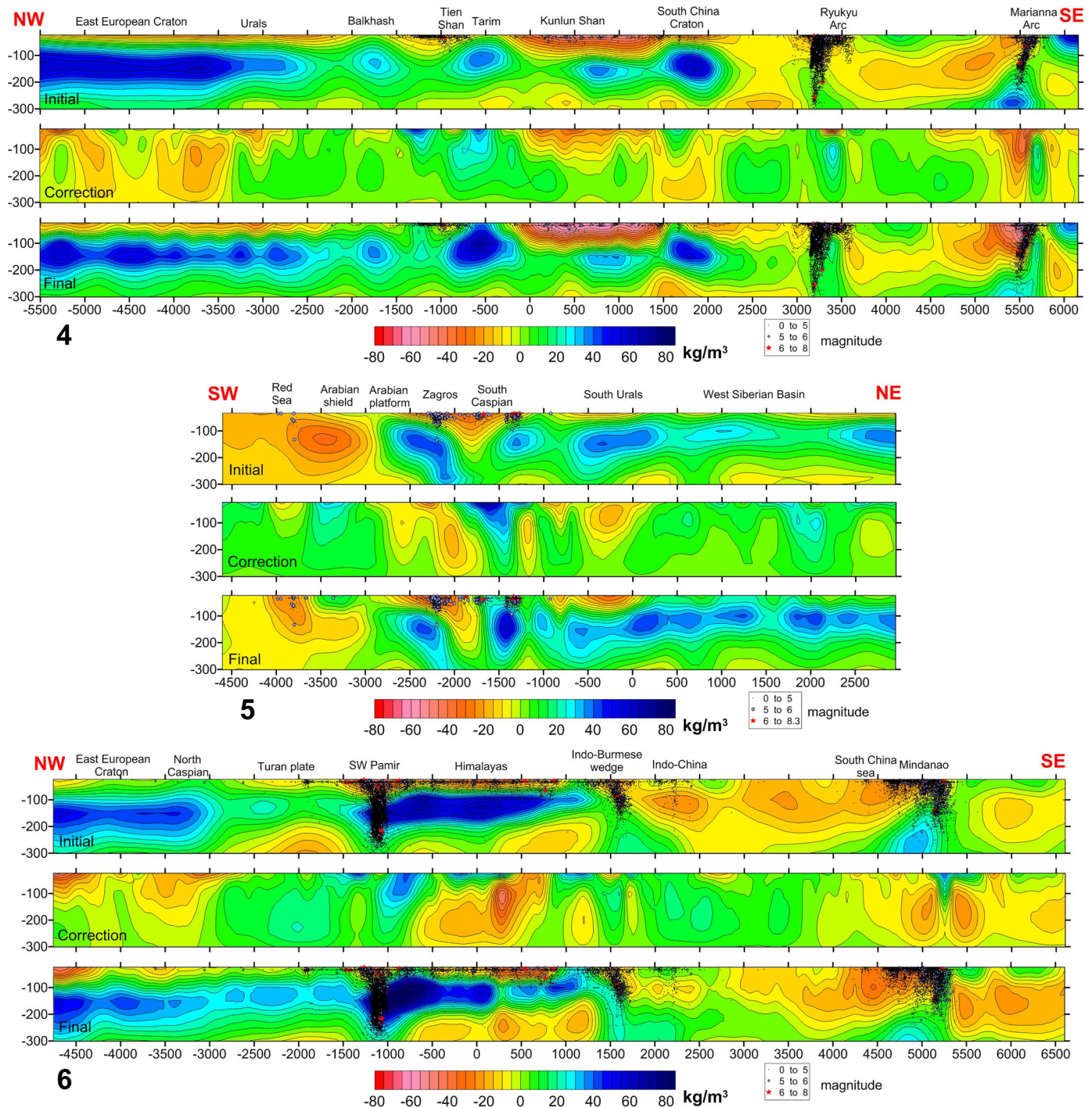


Figure 8. Location map and six cross sections showing the density structure of the upper mantle. The **initial** model is based on the SL2013sv tomography model [Schaeffer and Lebedev, 2013]. The **correction** was obtained by joint inversion of the residual mantle gravity and residual topography. The **final** model fits both residual gravity and topography and has minimal possible deviations from the initial model. Location of earthquake hypocenters with magnitude classification are plotted onto cross sections delineating different tectonic regimes, the earthquakes data are obtained from the ISC-GEM catalogue [Storchak et al., 2013]. The vertical scale is 3 times extended compared to the horizontal one except for the part of the first profile, in which the scale is equal.

a large part of the Siberian Craton (Figure 8, cross-section 2), which is somewhat less than that previously reported in studies based on interpretation of only the gravity field [e.g., Kaban et al., 2003] or on the modeling of the isostatic balance of the lithosphere [Cherepanova and Artemieva, 2015]. Again, this



difference may be a result of the damping in the inversion. Similar density variations were found for the East European Craton and the Urals (Figures 7 and 8, cross-section 4). We can conclude that only moderate variations of the upper mantle density related to compositional changes in the cratonic roots are sufficient to explain the observed fields. These results also indicate the possibility of testing the isopycnic hypothesis [Jordan, 1988], which suggests that the density increase caused by low temperatures is compensated by the density decrease beneath the cratons owing to depletion. We determined that isopycnicity is not completely satisfied for both the Siberian and East European cratons, where a maximum density decrease

of about 40 kg m^{-3} still exists at depths of 100–170 km (Figure 8, cross-sections 1, 2, and 4). This conclusion remains valid even when we consider the damping effect.

In South Asia, the Indian Craton is somewhat similar to the northern cratons, although the corresponding density variations are significantly less in the Indian craton than in the latter (Figure 8, cross-section 3). This craton is also characterized by additional decreases in density, which are likely related to the depleted root, and by a density decrease at a depth of about 100 km in the final model. In contrast, in the South China and Sino-Korean cratons, we estimated near-zero corrections to the initial model suggesting that the ancient low-density cratonic roots have been destroyed and replaced by juvenile mantle, as indicated by previous petrological and geological studies [Yang *et al.*, 2010; Kusky *et al.*, 2007; Zheng and Zhang, 2007].

The joint inversion of the residual gravity and residual topography substantially refined the tomography image of the oceanic subduction zones in the Western Pacific. This is clearly visible in regions where the seismic tomography model is not well constrained. For example, the Ryukyu and Marianna arcs are almost indistinguishable in the initial model but are visible after the inversion (Figure 8, cross-section 4). The location of the subducting slabs well corresponds to the distribution of the earthquake hypocenters, which delineate the boundaries of the slabs. The back-arc basins are both characterized by low-density anomalies in the uppermost mantle up to a maximum depth of about 150 km, likely reflecting the ascension of magma that feeds them. Remarkably more details can be distinguished in well-studied regions such as the Japan arc-trench system, where we observed important changes of the initial model after the inversion (Figure 8, cross-section 1). The final density model of the subducting slab was split in two parts: an upper high-density fragment extending to a depth of about 40–50 km and a lower one located below about 70 km. The edges of these fragments are clearly bounded by clusters of earthquakes confined to the subducting slab. The depth range of hypocenters and the dipping trend fit the final density model (Figure 8, cross-section 1). This does not necessarily imply that the slab is physically fragmented, although it indicates that the intermediate part is neutrally buoyant relative to the surrounding material. We can speculate that the fluids derived by slab dehydration cause serpentinization of the slab and consequently the decrease in density at this depth, as already hypothesized in previous studies [e.g., Hyndman and Peacock, 2003]. Furthermore, the lower part is substantially denser and thicker relative to the initial model (Figure 8, cross-section 1). Hacker *et al.* [2003] predicted the formation of anhydrous eclogites in the mantle lithosphere of a subducting slab below about 80 km. These rocks are almost indistinguishable by seismic velocity but have up to about 6% increased density. Therefore, Hacker *et al.* [2003] suggested that eclogites can be detected by gravity modeling. Our results confirm their hypothesis.

For intracontinental collision zones such as the Himalayas and the Zagros fold belt, the inversion mainly improved the resolution of the initial model but did not produce significant changes (Figure 8, cross-sections 2 and 5). The low-density upper mantle beneath the Tibetan Plateau was also well resolved in the initial model (Figure 8, cross-section 2). This proves that the initial velocity-temperature-density conversion is consistent for these structures and that the main density changes are related to temperature variation. The same conclusion can be made for the Altay-Sayan fold region and for the Trans-Baikal zone, a mountainous region to the east of the Lake Baikal, (Figure 8, cross-section 2), which are essentially characterized by low-density mantle up to a depth of about 150 km likely related to a hot and thin lithosphere [e.g., Bushenkova *et al.*, 2002]. In contrast, the Indo-Burmese wedge is not visible in the tomography model, but appears in the adjusted density model showing the subducting lithosphere in agreement with the earthquake hypocenters, the dipping direction of seismicity, the hypocenters step plane pattern, and the depth of occurrence clearly coincide with the Indian slab (Figure 8, cross-section 6).

For intracontinental orogenic belts, a significant negative correction of the mantle density was obtained only in the uppermost mantle, at about 100 km, for the western Tien Shan and northern Pamir mountains (Figure 7), approximately north of the boundary marking the subduction of the lithosphere of Asia beneath the central Pamirs [Fan *et al.*, 1994]. The subduction zone is associated with the dense mantle rocks south of this boundary (Figure 7c). It is significantly deepened compared to the initial model in agreement with the earthquakes' location trend. The focal depth of earthquake clusters and the background seismicity level are associated with the subduction zone indicating an intriguing geometry with its configuration (Figure 8, cross-section 6). For the negative anomaly to the north, it is still an open question whether this correction is related to fundamental properties of the lithosphere such as compositional differences or whether it only improved the resolution of the initial model based on seismic tomography.

In agreement with the previous study of *Kaban et al.* [2016], the inversion significantly improved the density structure of the Arabian plate and the Red Sea. The Arabian plate is divided in two distinct parts characterized by a reversed vertical dipole structure, the Arabian Shield and Arabian Platform. The uppermost mantle of the Arabian Shield has a normal density, whereas it is underlain by low-density material below a depth of about 100 km (Figures 7c and 8, cross-section 5). This low-density zone is connected with the localized hot-mantle anomaly beneath the Red Sea, as also observed in regional seismic tomography [e.g., *Chang and Van der Lee*, 2011]. In contrast, the uppermost mantle in the central part of the Arabian platform has relatively low density, which might be associated with the presence of depleted material [*Priestley et al.*, 2012]. Below this anomaly, the high density zone extends to a depth of about 200 km, which corresponds to the bottom of the lithosphere in the Arabian platform. The Red Sea is clearly divided in two parts: a low-density zone limited to a depth of about 150 km in the northern part and extending to the bottom of the model in the southern part. The latter is likely connected to the upwelling mantle plume (Figures 7c and 8, cross-section 5).

Several sedimentary basins of onshore regions, such as the Tarim and South Caspian basins, and offshore areas, such as the Barents Sea, the Bay of Bengal, and, to some extent, the northwestern part of the Okhotsk Sea, are underlain by very dense upper mantle (Figures 7c and 8, cross-sections 3, 4, and 5). Furthermore, these anomalies were significantly increased over those in the initial model after the inversion, particularly in the South Caspian and Tarim basins, and in the NW Okhotsk Sea, as shown in Figure 8, cross-sections 5, 4, and 3, respectively. The largest anomalies under the South Caspian and Tarim basins are clearly delineated by clusters of earthquakes. The presence of high-density material is at least partly related to compositional changes. High-density anomalies were previously reported beneath the Gulf of Mexico by *Mooney and Kaban* [2010] and *Kaban et al.* [2014b] and Barents Sea by *Ebbing et al.* [2007], *Braitenberg and Ebbing* [2009], and *Gac et al.* [2014]. *Mooney and Kaban* [2010] hypothesized that this anomaly is related to large bodies of eclogites in the subcrustal layer, which are much more easily detectable in the gravity field than in seismic velocity. In the present study, this feature has been consistently observed beneath many sedimentary basins. Therefore, the gabbro-eclogite transformation plays an important role in their evolution and usually causes rapid subsidence [e.g., *Kaus et al.*, 2005].

7. Conclusions

The conclusions of this study are summarized as follows:

1. An integrative density model of the crust and upper mantle was constructed for Asia and its surrounding areas. The gravity field data, recent crustal and seismic tomography models, and mineral physics constraints were used to identify the upper mantle features. As the first step, a comprehensive model of the crust [*Stolk et al.*, 2013] was employed to remove the impact of the crust on the observed gravity field and topography variations and to calculate the residual mantle gravity anomalies and residual topography. The variations of the residual gravity and residual topography range from -400 to $400 \times 10^{-5} \text{ m/s}^2$ (mGal) and from -4 km to more than 5 km, respectively. These fields represent the density heterogeneity of the mantle and can be used as a starting point in various studies of the Earth's structure and dynamics.
2. A new technique using both residual gravity and residual topography was employed to invert the residual fields for a 3D density model of the mantle. The inversion was constrained by the initial density model estimated by using a recent seismic tomography model [*Schaeffer and Lebedev*, 2013]. The corrections to the initial model, ranging from about -50 to 50 kg/m^3 , improved the resolution of the initial model and revealed several main features of the upper mantle that were not sufficiently resolved by seismic tomography. These perturbations to the initial model should be considered as a lower limit due to the damping that is implicitly present in the inversion.
3. The most significant negative density anomalies, which complement the initial model, are observed in the Siberian and East European cratons located in the northern part of the study area. These anomalies are associated mainly with the mantle material depleted in Fe components. The maximum amplitude of the density reduction is about 45 kg/m^3 (1.35%) at a depth of about 100 km. However, the decrease of density does not completely compensate the effect of low temperature even if we consider possible effects of the damping. We still observe increased values up to 40 kg/m^3 at depths of 100–170 km

beneath these cratons. Therefore, the isopycnic hypothesis of *Jordan* [1988] is not completely fulfilled. The structure of the Indian Craton is similar to that of the northern cratons, although it is characterized by substantially lower amplitudes of the density anomalies.

4. For the South China and Sino-Korean cratons, the initial density structure is different from the northern cratons. It is characterized by slightly negative anomalies down to a depth of about 100 km. However, for both cratons, the correction to the initial density, which is in most of the cases related to compositional heterogeneity, was negligible. Thus, the original, buoyant roots of the cratons have been replaced by juvenile mantle of higher density.
5. The density structure of the Western Pacific subduction zones was substantially refined in the inversion of the residual gravity and topography. The final model of the Japan Arc shows density variations of the subducting slab with depth. The upper part extends to a depth of about 40–50 km and is characterized by high density. The intermediate part down to about 70 km is neutrally balanced with the surrounding mantle, whereas the lower part is remarkably thicker and denser than that in the initial model. This difference is likely related to metamorphic reactions that caused dehydration of the slab at intermediate depths and its eclogitization below 80 km. The location of the hypocenters and the seismicity pattern clearly delineate the major structural features of the final density model.
6. For most mountain regions in Central and South Asia, we did not detect significant perturbations from the initial model. Therefore, the velocity-temperature-density conversion is consistent in these structures, and most of the density changes may be related to temperature anomalies. An exception is the Indo-Burmese wedge, where the joint inversion revealed the image of the subducting continental lithosphere. Significant changes were also detected in the Pamir region in agreement with the seismicity pattern.
7. This study confirms that the Arabian plate is composed of two parts: the Arabian shield and the Arabian platform, which are characterized by different density structures of the upper mantle. In the shield, the uppermost mantle is not anomalous in density, while below about 100 km, it is underlain by hot material of low density. To the west, this zone is connected to the hot mantle channel beneath the Red Sea. In contrast, the normal lithosphere extends to a depth of at least 200 km beneath the Arabian platform. In the central part of the platform, we obtained a negative density correction in the uppermost layer, which is possibly related to partially depleted material.
8. The largest high density of the upper mantle was observed beneath deep sedimentary basins, including those of the Tarim, South Caspian, and Barents seas, the Bay of Bengal, and, to some extent, the north-western part of the Okhotsk Sea. Notably, these anomalies were not effectively resolved in the initial model, although they became significant in the inversion of the residual gravity and residual topography. We attribute these results to eclogite bodies in the uppermost mantle, which are significantly denser than the normal mantle and have likely accelerated the subsidence of these basins.

Acknowledgments

We thank reviewers and editors for their extensive comments that have greatly improved this paper. This study was funded by GeoForschungsZentrum, Potsdam, Utrecht University, the Netherlands Research Centre for Integrated Solid Earth Science (ISES-2014-UU-08 and ISES-2016-UU-19), and in part by the Netherlands Space Organisation (SRON/NSO). The authors extend their appreciation to the Deanship of Scientific Research at King Saud University, Saudi Arabia, for funding the research group project (RG-1435-027). S. Cloetingh thanks the Alexander von Humboldt Foundation for their award. The results of this study are available in digital form from GFZ Potsdam (kaban@gfz-potsdam.de).

References

- Afonso, J. C., M. Fernández, G. Ranalli, W. L. Griffin, and J. A. D. Connolly (2008), Integrated geophysical-petrological modeling of the lithosphere and sublithospheric upper mantle: Methodology and applications, *Geochem. Geophys. Geosyst.*, 9, Q05008, doi:10.1029/2007GC001834.
- Anderson, D. L., and J. D. Bass (1984), Mineralogy and composition of the upper mantle, *Geophys. Res. Lett.*, 11(7), 637–640.
- Artemjev, M. E., M. K. Kaban, V. A. Kuchnerenko, G. V. Demjanov, and V. A. Taranov (1994), Subcrustal density inhomogeneities of Northern Eurasia as derived from the gravity data and isostatic models of the lithosphere, *Tectonophysics*, 240, 249–280.
- Artemieva, I., H. Thybo, and M. Kaban (2006), Deep Europe today: Geophysical synthesis of the upper mantle structure and lithospheric processes over 3.5 By, in *European Lithosphere Dynamics*, edited by D. Gee and R. Stephenson, vol. 32, pp. 11–41, Geol. Soc. London Mem., London, U. K.
- Artemieva, I. M. (2009), The continental lithosphere: Reconciling thermal, seismic, and petrologic data, *Lithos*, 109(1), 23–46.
- Bai, Z., S. Zhang, and C. Braitenberg (2013), Crustal density structure from 3D gravity modeling beneath Himalaya and Lhasa blocks, *Tibet. J. Asian Earth Sci.*, 78, 301–317.
- Basuyau, C., M. Diamant, C. Tiberi, G. Hetényi, J. Vergne, and A. Peyrefitte (2013), Joint inversion of teleseismic and GOCE gravity data: Application to the Himalayas, *Geophys. J. Int.*, 193(1), 149–160.
- Becker, J. J. et al. (2009), Global bathymetry and elevation data at 30 arc seconds resolution: SRTM30_PLUS, *Marine Geodesy*, 32(4), 355–371.
- Boschi, L., C. Faccenna, and T. W. Becker (2010), Mantle structure and dynamic topography in the Mediterranean Basin, *Geophys. Res. Lett.*, 37, L20303, doi:10.1029/2010GL045001.
- Braitenberg, C., and J. Ebbing (2009), The GRACE-satellite gravity field in analysing large scale, cratonic or intracratonic basins, *Geophys. Prospect.*, 57, 559–571, doi:10.1111/j.1365-2478.2009.00793.x.
- Braitenberg, C., M. Zadro, J. Fang, Y. Wang, and H. T. Hsu (2000a), The gravity and isostatic Moho undulations in Qinghai-Tibet plateau, *J. Geodyn.*, 30(5), 489–505.
- Braitenberg, C., M. Zadro, J. Fang, Y. Wang, and H. T. Hsu (2000b), Gravity inversion in Qinghai-Tibet plateau, *Phys. Chem. Earth, Part A*, 25(4), 381–386.

- Braitenberg, C., S. Wienecke, and Y. Wang (2006), Basement structures from satellite-derived gravity field: South China Sea ridge, *J. Geophys. Res.*, **111**, B05407, doi:10.1029/2005JB003938.
- Bushenkova, N., S. Tychkov, and I. Koulakov (2002), Tomography on PP-P waves and its application for investigation of the upper mantle in central Siberia, *Tectonophysics*, **358**(1), 57–76.
- Cammarano, F., S. Goes, P. Vacher, and D. Giardini (2003), Inferring upper-mantle temperatures from seismic velocities, *Phys. Earth Planet. Inter.*, **138**, 197–222, doi:10.1016/S00319201(03)00156-0.
- Chang, S., and S. Van der Lee (2011), Mantle plumes and associated flow beneath Arabia and East Africa, *Earth Planet. Sci. Lett.*, **302**, 448–454.
- Chen, L., C. Cheng, and Z. Wei (2009), Seismic evidence for significant lateral variations in lithospheric thickness beneath the central and western North China craton, *Earth Planet. Sci. Lett.*, **286**(1), 171–183.
- Cherepanova, Y., and I. M. Artemieva (2015), Density heterogeneity of the cratonic lithosphere: A case study of the Siberian Craton, *Gondwana Res.*, **28**(4), 1344–1360.
- Christensen, N. I., and W. D. Mooney (1995), Seismic velocity structure and composition of the continental crust: A global review, *J. Geophys. Res.*, **100**, 9761–9788.
- Collins, C. D. N., B. J. Drummond, and M. G. Nicoll (2003), Crustal thickness patterns in the Australian continent, *Geol. Soc. Am. Bull.*, **372**, 121–128.
- Courtillot, V. A., X. Kravchinsky, P. R. Quidelleur, and D. P. Renne (2010), Gladkochub Preliminary dating of the Viluy traps (Eastern Siberia): Eruption at the time of Late Devonian extinction events?, *Earth Planet. Sci. Lett.*, **300**, 239–245.
- Delvaux, D., R. Moeys, G. Stapel, C. Petit, K. Levi, A. Miroshnichenko, V. Ruzhich, and V. San'kov (1997), Paleostress reconstructions and geodynamics of the Baikal region, central Asia, Part 2. Cenozoic rifting, *Tectonophysics*, **282**(1), 1–38.
- Divins, D. L. (2003), Total Sediment Thickness of the World's Oceans and Marginal Seas, NOAA Natl. Geophys. Data Cent., Boulder, Colo.
- Dong, Z., J. Tang, M. Unsworth, and X. Chen (2015), Electrical resistivity structure of the upper mantle beneath Northeastern China: Implications for rheology and the mechanism of craton destruction, *J. Asian Earth Sci.*, **100**, 115–131.
- Ebbing, J., C. Braitenberg, and S. Wienecke (2007), Insights into the lithospheric structure and the tectonic setting of the Barents Sea region from isostatic considerations, *Geophys. J. Int.*, **171**, 1390–1403, doi:10.1111/j.1365-246X.2007.03602.x.
- Exxon (1985), *Tectonic Map of the World*, pp. 16, Am. Assoc. of Pet. Geol., Tulsa, Okla.
- Faccenna, C., and T. W. Becker (2010), Shaping mobile belts by small-scale convection, *Nature*, **465**, 602–605, doi:10.1038/nature09064.
- Fan, G., J. F. Ni, and T. C. Wallace (1994), Active tectonics of the Pamirs and Karakorum, *J. Geophys. Res.*, **99**, 7131–7160.
- Flament, N., M. Gurnis, and R. D. Müller (2013), A review of observations and models of dynamic topography, *Lithosphere*, **5**(2), 189–210, doi:10.1130/L245.1.
- Forsberg, R., and C. C. Tscherning (1997), Topographic effects in gravity field modelling for BVP, in *Geodetic Boundary Value Problems in View of the One Centimeter Geoid*, pp. 239–272, Springer, Heidelberg.
- Förste, C., S. L. Bruinsma, F. Flechtner, J. Marty, J. M. Lemoine, C. Dahle, and G. Balmino (2012), A preliminary update of the Direct approach GOCE Processing and a new release of EIGEN-6C, in *AGU Fall Meeting Abstracts*, vol. 1, pp. 923, AGU, San Francisco.
- Förste, C., S. Bruinsma, O. Abrikosov, F. Flechtner, J. C. Marty, J. M. Lemoine, and R. Biancale (2014), EIGEN-6C4-The latest combined global gravity field model including GOCE data up to degree and order 1949 of GFZ Potsdam and GRGS Toulouse, in *EGU General Assembly Conference Abstracts*, May 2014, vol. 16, pp. 3707, EGU Vienna.
- Forte, A. M., and R. Peltier (1991), Viscous flow models of global geophysical observables: 1. Forward problems, *J. Geophys. Res.*, **96**, 20,131–20,159.
- Foulger, G. R., et al. (2013), Caveats on tomographic images, *Terra Nova*, **25**, 259–281.
- Gac, S., R. S. Huismans, N. S. C. Simon, J.-I. Faleide, and Y. Y. Podladchikov (2014), Effects of lithosphere buckling on subsidence and hydrocarbon maturation: A case-study from the ultra-deep East Barents Sea basin, *Earth Planet. Sci. Lett.*, **407**, 123–133.
- Gac, S., R. S. Huismans, N. S. C. Simon, J. Y. Y. Podladchikov, and J.-I. Faleide (2012), On the origin of the ultradeep East Barents Sea basin, *J. Geophys. Res.*, **117**, B04401, doi:10.1029/2011JB008533.
- Garzanti, E., and M. Gaetani (2002), Unroofing history of Late Paleozoic magmatic arcs within the “Turan Plate” (Turkmenistan), *Sediment. Geol.*, **151**, 67–87.
- Ghosh, A., T. W. Becker, and E. D. Humphreys (2013), Dynamics of the North American continent, *Geophys. J. Int.*, **194**, 651–669.
- Goes, S., and S. van der Lee (2002), Thermal structure of the North American uppermost mantle inferred from seismic tomography, *J. Geophys. Res.*, **107**(B3), doi:10.1029/2000JB000049.
- Goes, S., R. Govers, and P. Vacher (2000), Shallow upper mantle temperatures under Europe from P and S wave tomography, *J. Geophys. Res.*, **105**, 11,153–11,169.
- Griffin, W. L., Z. Andi, S. Y. O'Reilly, and C. G. Ryan (1998), Phanerozoic evolution of the lithosphere beneath the Sino-Korean craton, in *Mantle Dynamics and Plate Interactions in East Asia*, *Geodyn. Ser.*, vol. 27, edited by M. F. J. Flower, S.-L. Chung, C.-H. Lo, and T.-Y. Lee, pp. 107–126, AGU, Washington, D. C.
- Griffin, W. L., C. G. Ryan, F. V. Kaminsky, S. Y. O'Reilly, L. M. Natapov, T. T. Win, and I. P. Ilupin (1999), The Siberian lithosphere traverse: Mantle terranes and the assembly of the Siberian Craton, *Tectonophysics*, **310**(1), 1–35.
- Griffin, W. L., L. M. Natapov, S. Y. O'Reilly, E. van Achterbergha, A. F. Cherenkovac, and V. G. Cherenkovc (2005), The Kharamai kimberlite field, Siberia: Modification of the lithospheric mantle by the Siberian Trap event, *Lithos*, **81**, 167–187.
- Gu, Y. J., A. M. Dziewonski, and G. Ekström, (2003), Simultaneous inversion for mantle shear velocity and topography, *Geophys. J. Int.*, **154**, 559–583.
- Hacker, B. R., G. A. Abers, and S. M. Peacock (2003), Subduction factory 1. Theoretical mineralogy, densities, seismic wave speeds, and H₂O contents, *J. Geophys. Res.*, **108**(B1), 2029, doi:10.1029/2001JB001127.
- Hackney, R. I., and W. E. Featherstone (2003), Geodetic versus geophysical perspectives of the ‘gravity anomaly’, *Geophys. J. Int.*, **154**(1), 35–43.
- Hyndman, R. D., and S. M. Peacock (2003), Serpentinization of the forearc mantle, *Earth Planet. Sci. Lett.*, **212**, 417–432.
- Jordan, T. H. (1978), Composition and development of the continental tectosphere, *Nature*, **274**(5671), 544–548.
- Jordan, T. H. (1988), Structure and formation of the continental tectosphere, *J. Petrol.*, (1), 11–37.
- Kaban, M. K., P. Schwintzer, and S. A. Tikhotsky (1999), A global isostatic gravity model of the Earth, *Geophys. J. Int.*, **136**(3), 519–536.
- Kaban, M. (2001), A gravity model of the North Eurasia Crust and Upper Mantle: 1. Mantle and isostatic residual gravity anomalies, *Russ. J. Earth Sci.*, **3**(2), 143–163.
- Kaban, M. K., and V. Trubitsyn (2012), Density structure of the mantle transition zone and the dynamic geoid, *J. Geodyn.*, **59–60**, 183–192.

- Kaban, M. K., and T. R. Yuanda (2014), Density structure, isostatic balance and tectonic models of the Central Tien Shan, *Surv. Geophys.*, **35**, 1375–1391, doi:10.1007/s10712-014-9298-7.
- Kaban, M. K., P. Schwintzer, I. M. Artemieva, and W. D. Mooney (2003), Density of the continental roots: Compositional and thermal contributions, *Earth Planet. Sci. Lett.*, **209**, 53–69.
- Kaban, M. K., P. Schwintzer, and Ch. Reigber (2004), A new isostatic model of the lithosphere and gravity field, *J. Geod.*, **78**, 368–385.
- Kaban, M. K., M. Tesauro, and S. Cloetingh (2010), An integrated gravity model for Europe's crust and upper mantle, *Earth Planet. Sci. Lett.*, **296**, 195–209, doi:10.1016/j.epsl.2010.04.041.
- Kaban, M. K., A. G. Petrunin, H. Schmeling, and M. Shahraki (2014a), Effect of decoupling of lithospheric plates on the observed geoid, *Surv. Geophys.*, **35**, 1361–1373, doi:10.1007/s10712-014-9281-3.
- Kaban, M. K., M. Tesauro, W. D. Mooney, and S. A. P. L. Cloetingh (2014b), Density, temperature, and composition of the North American lithosphere—New insights from a joint analysis of seismic, gravity, and mineral physics data: 1. Density structure of the crust and upper mantle, *Geochem. Geophys. Geosyst.*, **15**, 4781–4807, doi:10.1002/2014GC005483.
- Kaban, M. K., W. D. Mooney, and A. G. Petrunin (2015a), Cratonic root beneath North America shifted by basal drag from the convecting mantle, *Nat. Geosci.*, **8**(10), 797–800, doi:10.1038/ngeo2525.
- Kaban, M. K., S. El Khrepy, and N. Al-Arifi (2015b), Isostatic model and isostatic gravity anomalies of the Arabian plate and surroundings, *Pure Appl. Geophys.*, 1211–1221, doi:10.1007/s00024-015-1164-0.
- Kaban, M. K., S. El Khrepy, N. Al-Arifi, M. Tesauro, and W. Stolk (2016), 3D density model of the upper mantle in the Middle East: Interaction of diverse tectonic processes, *J. Geophys. Res.*, **121**, 5349–5364, doi:10.1002/2015JB012755.
- Kaus, B. J., J. A. Connolly, Y. Y. Podladchikov, and S. M. Schmalholz (2005), Effect of mineral phase transitions on sedimentary basin subsidence and uplift, *Earth Planet. Sci. Lett.*, **233**(1), 213–228.
- Kusky, T. M., B. F. Windley, and M. G. Zhai (2007), Tectonic evolution of the North China Block: From orogen to craton to orogen, *Geol. Soc. Spec. Publ.*, **280**(1), 1–34.
- Larson, K. M., R. Burgmann, R. Bilham, and J. T. Freymueller (1999), Kinematics of the India-Eurasia collision zone from GPS measurements, *J. Geophys. Res.*, **104**, 1077–1093.
- Laske, G., G. Masters, Z. Ma, and M. Pasyanos (2013), Update on CRUST1.0—A 1-degree global model of Earth's crust, *Geophys. Res. Abstr.*, **15** (Abstract EGU2013-2658, 2013).
- Li, X., and H. J. Götze (2001), Ellipsoid, geoid, gravity, geodesy, and geophysics, *Geophysics*, **66**(6), 1660–1668.
- Logatchev, N. A., and N. A. Florensov (1978), The Baikal system of rift valleys, *Tectonophysics*, **45**(1), 1–13.
- Maceira, M., and C. J. Ammon (2009), Joint inversion of surface wave velocity and gravity observations and its application to central Asian basins shear velocity structure, *J. Geophys. Res.*, **114**, B02314, doi:10.1029/2007JB005157.
- Maurin T., and C. Rangin (2009), Structure and kinematics of the Indo-Burmese Wedge: Recent and fast growth of the outer wedge, *Tectonics*, **28**, TC2010, doi:10.1029/2008TC002276.
- McDonough, W. F., and S.-S. Sun (1995), The composition of the Earth, *Chem. Geol.*, **120**, 223–253.
- Molnar, P., and P. Tapponnier (1975), Cenozoic tectonics of Asia: Effects of a continental collision, *Science*, **189**(4201), 419–426.
- Mooney, W. D. (2010), 11 crust and lithospheric structure-global crustal structure, *Seismol. Struct. Earth Treat. Geophys.*, **1**, 361.
- Mooney, W. D., and M. K. Kaban (2010), The North American Upper Mantle: Density, composition, and evolution, *J. Geophys. Res.*, **115**, B12424, doi:10.1029/2010JB000866.
- Nutman, A. P., I. V. Chernyshev, H. Baadsgaard, and A. P. Smelov (1992), The Aldan Shield of Siberia, USSR: The age of its Archaean components and evidence for widespread reworking in the mid-Proterozoic, *Precambrian Res.*, **54**, 195–210.
- Petit, C., and J. Deverchere (2006), Structure and evolution of the Baikal rift: A synthesis, *Geochem. Geophys. Geosyst.*, **7**, Q11016, doi:10.1029/2006GC001265.
- Petrunin, A. G., M. K. Kaban, I. Rogozhina, and V. Trubitsyn (2013), Revising the spectral method as applied to modeling mantle dynamics, *Geochem. Geophys. Geosyst.*, **14**, 3691–3702, doi:10.1002/ggge.20226.
- Priestley, K., D. McKenzie, J. Barron, M. Tatar, and E. Debayle (2012), The Zagros core: Deformation of the continental lithospheric mantle, *Geochem. Geophys. Geosyst.*, **13**, Q11014, doi:10.1029/2012GC004435.
- Puchkov, V. (2002), Paleozoic evolution of the East European Continental Margin involved in the Uralide Orogeny, in *Mountain Building in the Uralides: Pangea to the Present*, edited by D. Brown, C. Juhlin, and V. Puchkov, AGU, Washington, D. C., doi:10.1029/132GM02.
- Rosen, O. M., K. C. Condie, L. M. Natapov, and A. D. Nozhdin (1994), Archean and Early Proterozoic evolution of the Siberian craton: A preliminary assessment, *Archean Crustal Evolution*, **11**, 411–459.
- Rowley, D. B. (1996), Age of initiation of collision between India and Asia: A review of stratigraphic data, *Earth Planet. Sci. Lett.*, **145**(1), 1–13.
- Rundqvist, D. V., and F. P. Mitrofanov (1993), *Precambrian Geology of the USSR*, vol. 9, pp. 247–263.
- Schaeffer, A. J., and S. Lebedev (2013), Global shear-speed structure of the upper mantle and transition zone, *Geophys. J. Int.*, **194**(1), 417–449.
- Schaeffer, A. J., and S. Lebedev (2014), Imaging the North American continent using waveform inversion of global and US Array data, *Earth Planet. Sci. Lett.*, **402**, 26–41.
- Sengör, A. M. C., B. A. Natal'in, and V. S. Burtman (1993), Evolution of the Altaid tectonic collage and Palaeozoic crustal growth in Eurasia, *Nature*, **364**, 299–307.
- Shin, Y. H., H. Xu, C. Braitenberg, J. Fang, and Y. Wang (2007), Moho undulations beneath Tibet from GRACE-integrated gravity data, *Geophys. J. Int.*, **170**(3), 971–985.
- Steinberger, B., and A. R. Calderwood (2006), Models of large-scale viscous flow in the Earth's mantle with constraints from mineral physics and surface observations, *Geophys. J. Int.*, **167**, 1461–1481.
- Stern, R. J., and P. Johnson (2010), Continental lithosphere of the Arabian Plate: A geologic, petrologic, and geophysical synthesis, *Earth Sci. Rev.*, **101**, 29–67.
- Stixrude, L., and C. Lithgow-Bertelloni (2005), Thermodynamics of mantle minerals—I. Physical properties, *Geophys. J. Int.*, **162**, 610–632.
- Stolk, W., M. K. Kaban, F. Beekman, M. Tesauro, W. D. Mooney, and S. Cloetingh (2013), High resolution regional crustal models from irregularly distributed data: Application to Asia and adjacent areas, *Tectonophysics*, **602**, 55–68.
- Storchak, D. A., D. Di Giacomo, I. Bondár, E. R. Engdahl, J. Harris, W. H. K. Lee, A. Villaseñor, and P. Bormann (2013), Public release of the ISC-GEM global instrumental earthquake catalogue (1900–2009), *Seismol. Res. Lett.*, **84**(5), 810–815, doi:10.1785/0220130034.
- Tesauro, M., M. K. Kaban, and S. A. P. L. Cloetingh (2008), EuCRUST-07: A new reference model for the European crust, *Geophys. Res. Lett.*, **35**, L05313, doi:10.1029/2007GL032244.
- Tesauro, M., M. K. Kaban, W. D. Mooney, and S. A. P. L. Cloetingh (2014a), Density, temperature, and composition of the North American lithosphere—New insights from a joint analysis of seismic, gravity, and mineral physics data: 2. Thermal and compositional model of the upper mantle, *Geochem. Geophys. Geosyst.*, **15**, 4808–4830, doi:10.1002/2014GC005484.

- Tesauero, M., M. K. Kaban, W. D. Mooney, and S. A. P. L. Cloetingh (2014b), NACr14: A 3D model for the crustal structure of the North American Continent, *Tectonophysics*, 631, 65–86.
- Tesauero, M., M. K. Kaban, and W. D. Mooney (2015), Variations of the lithospheric strength and elastic thickness in North America, *Geochem. Geophys. Geosyst.*, 16, 2197–2220, doi:10.1002/2015GC005937.
- Tiberi, C., A. Deschamps, J. Déverchère, C. Petit, J. Perrot, D. Appriou, and A. A. Artemiev (2008), Asthenospheric imprints on the lithosphere in Central Mongolia and Southern Siberia from a joint inversion of gravity and seismology (MOBAL experiment), *Geophys. J. Int.*, 175(3), 1283–1297.
- Tikhonov, A. N., and V. Y. Arsenin (1977), *Solutions of Ill-Posed Problems*, V. H. Winston (Ed.), John Wiley, N. Y.
- Vyssotski, A. V., V. N. Vyssotski, and A. A. Nezhdanov (2006), Evolution of the West Siberian Basin, *Mar. Pet. Geol.*, 23, 93–126.
- White, L. T., and G. S. Lister (2012), The collision of India with Asia, *J. Geodyn.*, 56, 7–17.
- Yang, J. H., S. O'Reilly, R. J. Walker, W. Griffin, F. Y. Wu, M. Zhang, and N. Pearson (2010), Diachronous decratonization of the Sino-Korean craton: Geochemistry of mantle xenoliths from North Korea, *Geology*, 38(9), 799–802.
- Yin, A. (2010), Cenozoic tectonic evolution of Asia: A preliminary synthesis, *Tectonophysics*, 488, 293–325.
- Zhang, Z., J. Teng, F. Romanelli, C. Braitenberg, Z. Ding, X. Zhang, L. Fang, S. Zhang, J. Wu, and Y. Deng (2014), Geophysical constraints on the link between cratonization and orogeny: Evidence from the Tibetan Plateau and the North China Craton, *Earth Sci. Rev.*, 130, 1–48.
- Zheng, Y., and S. Zhang (2007), Formation and evolution of Precambrian continental crust in South China, *Chinese Sci. Bull.*, 52(1), 1–12.
- Zheng, J., S. Y. O'Reilly, W. L. Grin, F. Lu, and M. Zhang (1998), Nature and evolution of cenozoic lithospheric mantle beneath Shandong Peninsula, Sino-Korean Craton, Eastern China, *Int. Geol. Rev.*, 40(6), 471–499.
- Zhou, B., J. S. Zhu, and K. Y. Chun (1991), Three-dimensional shear velocity structure beneath Qinhai-Tibet and its adjacent area, *Acta Geophys. Sin.*, 34(4), 426–441.